CRYOGENIC SHAPE MEMORY ALLOY ACTUATORS FOR SPACEPORT TECHNOLOGIES: MATERIALS CHARACTERIZATION AND PROTOTYPE TESTING

by

JENNIFER L. LEMANSKI
B.A. University of Central Florida, 1995
B.S. University of Central Florida, 2003

A thesis submitted in partial fulfillment of the requirements
for the degree of Master of Science
in the Department of Mechanical, Materials and Aerospace Engineering
in the College of Engineering
at the University of Central Florida
Orlando, Florida

Spring Term
2005

ABSTRACT

Shape memory alloys (SMAs) possess the unique ability to change their shape by undergoing a solid-state phase transformation at a particular temperature. The shape change is associated with a large strain recovery as the material returns to its "remembered" shape. Their ability to act as both sensor and actuator has made them an attractive subject of study for numerous applications. SMAs have many characteristics which are advantageous in space-related applications, including generation of large forces associated with the strain recovery, smooth and controlled movements, large movement to weight ratio, high reliability, and spark-free operation. The objective of this work is the further development and testing of a cryogenic thermal conduction switch as part of NASA funded projects. The switch was developed to provide a variable conductive pathway between liquid methane and liquid oxygen dewars in order to passively regulate the methane temperature. Development of the switch concept has been continued in this work by utilizing Ni-Ti-Fe as the active SMA element. Ni-Ti-Fe exhibits the shape memory effect at cryogenic temperatures, which makes it well suited for low temperature applications. This alloy is also distinguished by an intermediate phase change known as the rhombohedral or R-phase, which is characterized by a small hysteresis (typically 1-2 deg C) and offers the advantage of precise control over a set temperature range. For the Ni-Ti-Fe alloy used, its thermomechanical processing, subsequent characterization using dilatometry and differential scanning calorimetry and implementation in the conduction switch configuration are addressed. This work was funded by grants from NASA KSC (NAG10-323) and NASA GRC (NAG3-2751).

Dedicated to my husband,

whose unfailing love and encouragement

helped make this dream a reality.

ACKNOWLEDGMENTS

I would first and foremost like to express my gratitude to my advisor and friend, Dr. Raj Vaidyanathan, for his invaluable advice and support throughout my thesis projects and research, his guidance and encouragement through the course of my graduate studies, and most importantly, for introducing me to shape-memory alloys four years ago which inspired me and changed the course of my career.

My gratitude also extends to Bill Notardonato for his helpful advice on cryogenics handling, for all his help during the dilatometer commissioning, and for serving on my defense committee. Thanks also to Dr. Eric Petersen and Dr. C. Suryanarayana for serving on my defense committee. I would also like to thank my friend and colleague, Vinu Krishnan, for his help and advice, both near and far, in the lab and throughout this project. Thanks also to all my friends and colleagues in Dr. Raj's research group for their help at various times and for their collaborative efforts to share their wealth of knowledge and expertise on shape-memory alloys and materials characterization.

My sincere gratitude is also extended to AMPAC's own Ms. Karen Glidewell, Ms. Angela Yetter, Ms. Cindy Harle, Ms. Kari Stiles and Ms. Waheeda Illasarie for all their help in ordering project materials and submitting paperwork, for generally helping to maintain order and sanity, and doing it all with a smile and kind word. Thanks also to Richard Zotti in the CREOL machine shop for his sound mechanical expertise, and last-minute tweaks and fixes.

Most of all I would like to thank my husband for being there with love and patience and support through it all, and my family and friends for their constant love and encouragement throughout this odyssey of higher education.

TABLE OF CONTENTS

LIST OF FIGURES

LIST OF TABLES

LIST OF ACRONYMS/ABBREVIATIONS

DSC	Differential Scanning Calorimeter
EDM	Electrical Discharge Machining
LVDT	Linear Variable Differential Transducer
NASA	National Aeronautics and Space Administration
NiTi	Nickel Titanium (alloy)
Ni-Ti-Fe	Nickel Titanium Iron (alloy)
SMA	Shape Memory Alloy
SME	Shape-Memory Effect

CHAPTER ONE: INTRODUCTION

1.1 Motivation

The unique properties of Shape Memory Alloys (SMAs) have been widely investigated for both scientific and commercial use over the past 40 years. They have gained particular attention in the aerospace industry for their use as hydraulic line couplings, vibration dampers, fail-safe devices, adaptive structures and actuators. The nature of SMAs allows them to function simultaneously as both sensor and actuator, making simplicity of operation an attractive feature for applications requiring autonomous operation.

The motivation for this project stems from a NASA-KSC requirement for passive thermal control at cryogenic temperatures. A passive thermal conduction switch has been designed to regulate temperatures between liquid methane and liquid oxygen dewars. The switch, which uses SMA for the actuating elements, is required to conduct 8 W of heat between the liquid methane dewar at 118 K and liquid oxygen at 92 K. Such a switch could support autonomous fuel farm operation for a Mars mission, or may alternatively be used in earth-based cryogenic storage facilities. A prototype switch to demonstrate proof-of-concept was developed by Droney *et al*. [2003] which used a commercially available NiTi alloy and operated between an ice water mixture at 273 K and hot water at 338 K. The next version of the conduction switch was developed by V. Krishnan in 2003, which used NiTi strips that were thermomechanically treated to allow operation within the cryogenic range. The switch was further developed and tested in this work by replacing the NiTi strips with a Ni-Ti-Fe alloy. This alloy is characterized by operation in the cryogenic range, as well as by an additional phase transformation between

martensite and austenite that exhibits a very low hysteresis. For applications requiring precise temperature control, minimization of hysteresis is of prime importance.

Alternative methods for thermal actuators include thermostatic bimetals and wax actuators. While wax actuators are capable of large force output and controlled motion, they have a very slow response time in comparison with SMAs, as well as the extra requirement of sealing the piston mechanism [Tautzenberger 1990]. Bimetal devices, which generally have very low hysteresis, are limited by geometrical constraints and are not capable of producing large forces [Tautzenberger 1990]. A low-hysteresis shape memory alloy thermal actuator combines the most favorable attributes of these alternative methods.

1.2 Shape Memory Alloys

SMAs are a unique class of metals that possess the ability to "remember" a shape and return to that predetermined form upon heating it to a given temperature. This characteristic, known as the Shape Memory Effect (SME), is the result of a thermoelastic transformation as the material goes through a solid-state phase transformation from martensite to austenite. As the material recovers its shape, it does so with considerable force, which advocates the usefulness of SMAs as actuators. The effect was first discovered in a gold-cadmium alloy in 1951, and later found in a Ti-Ni alloy in 1963 [Otsuka & Wayman 1998]. The binary Ti-Ni alloys were developed by the Naval Ordnance Laboratory, and are commonly called Nitinol (Nickel Titanium Naval Ordnance Lab). Nitinol, which refers to any in a family of near equiatomic NiTi alloys, is frequently used in commercial and medical applications and is favored for its corrosion resistance, strength, and biocompatibility. In addition to SME, shape memory alloys exhibit

superelastic behavior when they are in the austenite phase, which is characterized by their ability to accommodate large amounts of strain (up to 8%) without permanent deformation of the material. Both the shape memory effect and superelasticity will be discussed in further detail in the next sections.

1.2.1 Shape Memory Effect

The shape memory effect is the name given to the macroscopic movement of shape memory alloys while undergoing a diffusionless, solid-state phase transformation from the martensite phase, which has a monoclinic lattice structure, to the austenite phase, which, for NiTi and Ni-Ti-Fe, is a BCC structure. The process is thermally activated, and can be characterized by four temperatures: M_s and M_f (martensite start and martensite finish) as the material cools from austenite to martensite, and similarly, A_s and A_f (austenite start and austenite finish) as the material undergoes the reverse transformation [Humbeeck 2001]. Figure 1.1 illustrates the shape memory effect. In Figure 1a, the spring is at a temperature above A_f and the lattice structure (shown above the spring) is cubic. As the spring cools below M_f (Figure 1.1b), the monoclinic martensite dominates. Note that the overall shape of the spring does not change between (a) and (b); the lower symmetry of the monoclinic structure results in twinning of the lattice planes, which does not produce a macroscopic shape change. If sufficient mechanical stress is applied (Figure 1.1c), semi-permanent deformation results. The strain in the material is accommodated by detwinning of the lattice planes into selected variants of martensite. When the deformed spring is heated to temperature A_f (Figure 1.1d), it recovers all the strain as the material once again returns to the austenite phase. The strain is completely recoverable because it is

accommodated by twinning, as opposed to slip, which is a permanent, destructive deformation of the lattice.

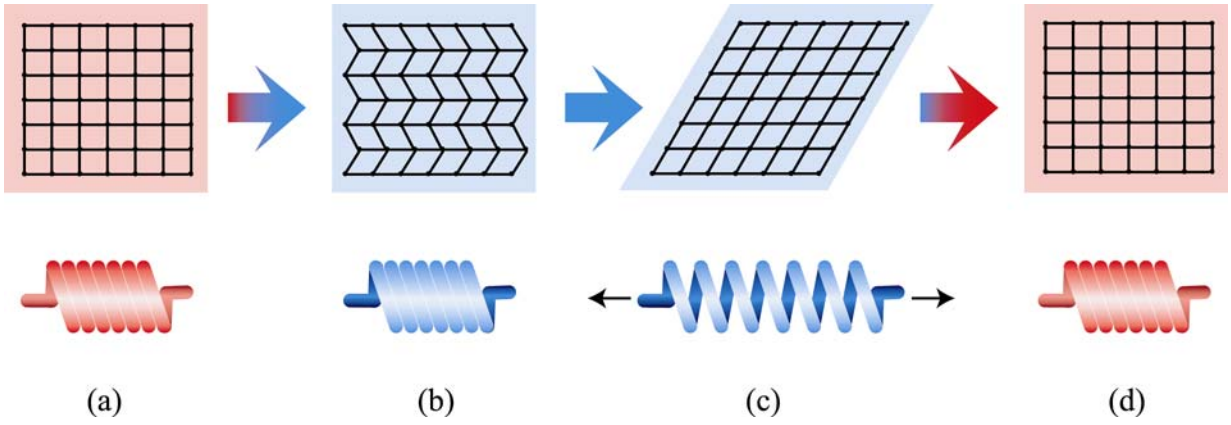

Figure 1.1: The Shape Memory Effect. (a) austenite phase crystal structure and undeformed spring; (b) twinned martensite crystal structure and undeformed spring; (c) detwinned martensite and macroscopic deformation; (d) shape recovery

The forward and reverse transformations (M_s and A_s) do not occur at the same temperatures, a phenomenon known as hysteresis. Typical hysteresis associated with shape memory alloys can be as much as 20-40 °C [Wayman & Duerig 1990]. The hysteretic effect is brought on by friction between twin boundaries as the atoms reorient themselves during the phase change [Wayman & Duerig 1990]. Figure 1.2 shows how property and temperature changes relate to hysteresis during the heating and cooling of a shape memory alloy. The hysteresis is typically measured by the difference between M_s and A_s for the forward and reverse transformations. For shape memory alloy actuator applications requiring precise temperature control, it is desirable to minimize hysteresis.

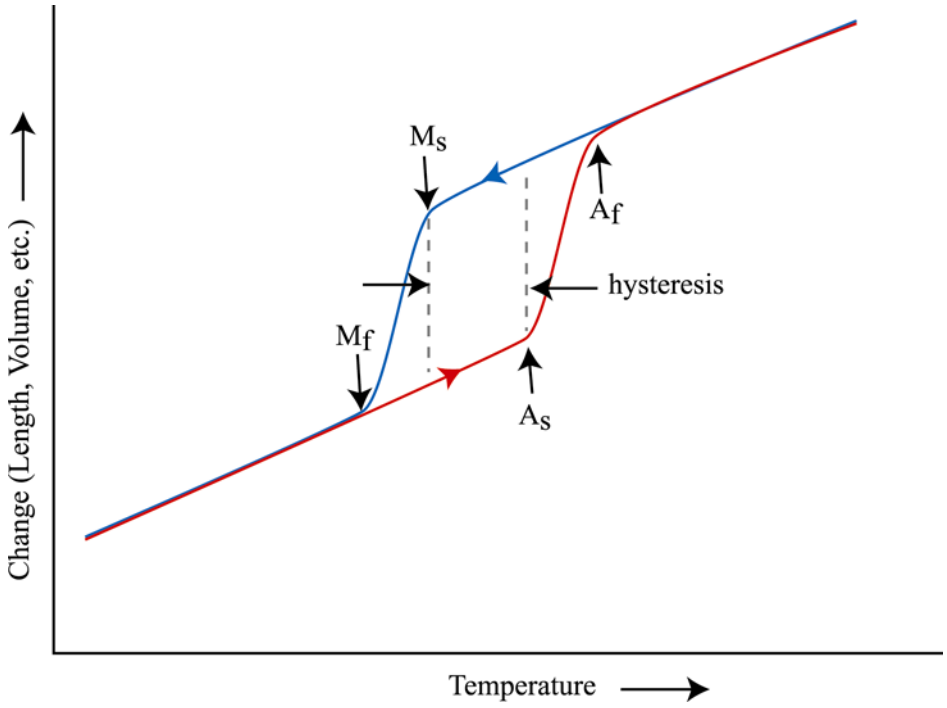

Figure 1.2: Hysteresis associated with phase transformation.

SME can be of two types: one-way and two-way. Figure 1.1, previously described above, illustrates the one-way shape memory effect. This can only be observed when some outside biasing force is applied to the spring to cause deformation. After the shape has recovered and the element is again cooled below M_f, no macroscopic movement is observed with the phase change. The two-way shape memory effect, however, has macroscopic movement associated with both heating and cooling. Figure 1.3 illustrates the two-way SME. As the spring is heated from martensite to austenite (Figure 1.3b to 1.3a), it returns to its "remembered" shape in the contracted state. Upon cooling back to martensite (Figure 1.3a to 1.3b), the spring moves to a second "remembered" shape.

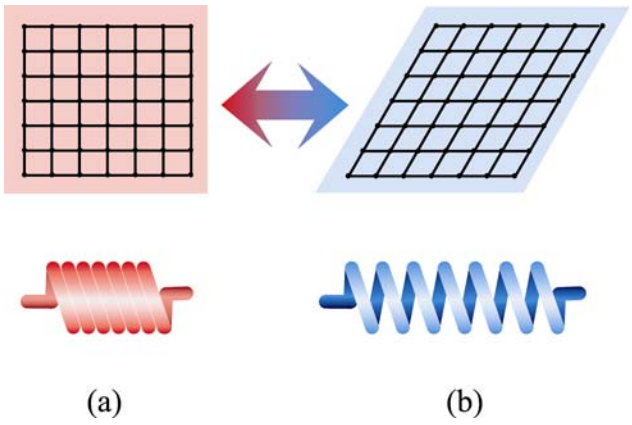

Figure 1.3: Two-way shape memory effect: (a) austenite; (b) martensite.

The two-way SME can be induced in an element by "training" the material utilizing such methods as plastic deformation, ageing under stress, thermal cycling, or use of precipitates [Otsuka & Wayman 1998]. Stresses and dislocations at the microscopic level are responsible for two-way shape memory [Wayman & Duerig 1990]. The dislocations stabilize the martensite, causing it to form in preferential directions each time the element is cooled [Otsuka & Wayman 1998]. The two-way SME has limitations, however, in actuator applications. While the force exerted against a load that is associated with the martensite to austenite phase change is comparable to the one-way shape memory effect, the force exerted during the reverse phase change is relatively weak [Perkins & Hodgson 1990].

1.2.2 Superelasticity

Superelasticity refers to the ability of shape memory alloys to accommodate a large amount of strain (up to 8%) without permanent plastic deformation. This characteristic has led to their wide use as cell phone antennas, cardiovascular stents, eyeglass frames, orthodontic wires,

and a variety of medical applications. The strain is accommodated by the preferential formation of stress-induced martensite (Figure 1.4b). Unlike the shape-memory effect where the martensite becomes stable due to a drop in temperature, this martensite is induced and stabilized by stress. Under stress conditions, only selected variants (directions) of martensite are formed which produce maximum elongation along the direction of the applied stress [Wayman & Duerig 1990]. When the applied stress is removed (Figure 1.4c), the alloy returns to its stable austenite phase, instantly recovering all the strain in the process.

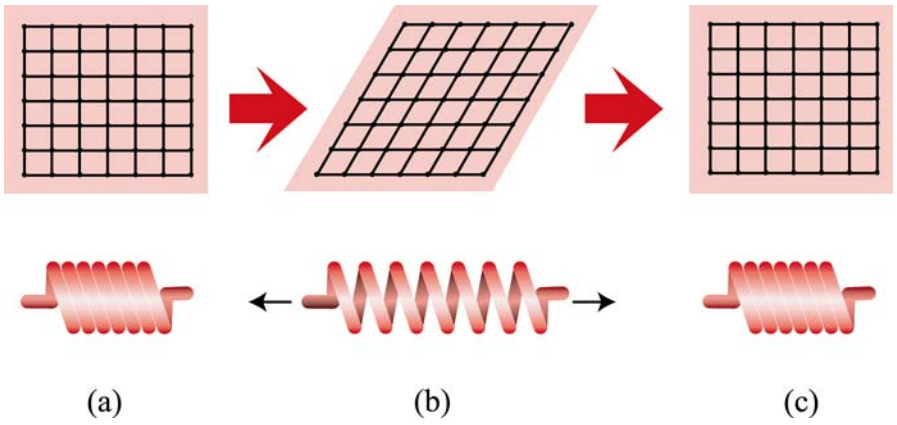

Figure 1.4: Superelasticity: (a) austenite; (b) stress-induced martensite; (c) shape recovery

1.3 Shape Memory Actuators

The ability of shape memory alloys to recover a large amount of strain against significant force makes them an appealing choice for actuator elements. SMA actuators are typically of two varieties: one-way and two-way. One-way actuators are designed to actuate only once, and have no opposing force to bring the actuated element back to its original position. This type of device

is typical of pipe couplings, safety devices and deployment mechanisms. Two-way actuators are designed to operate in two directions over many cycles, and can be of either a biased or a differential design. SMA elements in these actuators are commonly in a spring configuration in order to maximize the lateral movement associated with the phase change. Biased SMA actuators (Figure 1.5a) operate by utilizing the one-way shape memory effect of an SMA element to provide motion in one direction, and a biasing force, typically a spring, to provide motion in the opposing direction. The arrow in each of the figures indicates the spring providing the dominant force. When the SMA spring in the biased actuator is austenitic, it becomes stronger than the bias spring and forces the bias spring into a contracted position. When the SMA spring cools into the more compliant martensitic phase, the force from the bias spring overcomes the SMA spring,

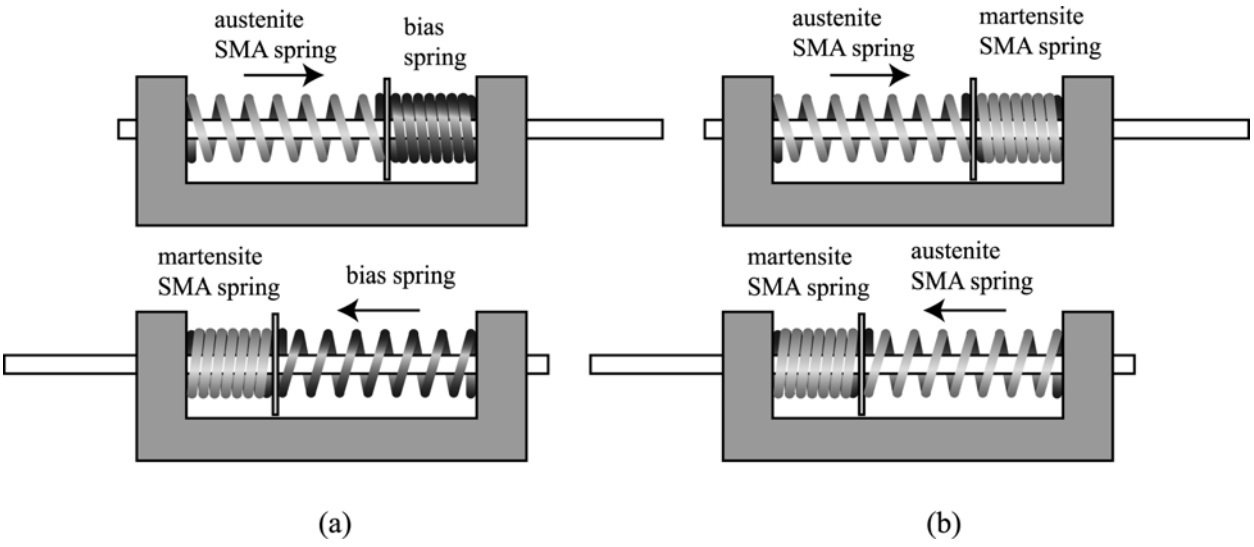

Figure 1.5: SMA actuator types: (a) biased SMA actuator, and (b) differential SMA actuator.

pushing it into a contracted position. The differential SMA actuator (Figure 1.5b) operates similarly, except that the bias spring is replaced by another SMA spring. One of the springs is

austenitic and the other is martensitic at all times, providing the back-and-forth motion. Biased actuators are commonly used in devices such as valves or switches, which require a two-position actuator that is either open or closed. Differential SMA actuators can be used in devices that require more precision motion control during the cycle. Additionally, SMA actuator elements can be in the form of strips, straight wires, and thin film coatings.

SMA actuators have the advantage of simplicity over other actuation devices in that the SMA element acts simultaneously as sensor and actuator. SMA actuation devices can operate either by direct exposure to a temperature change in its immediate environment, or by means of electrical resistance heating. This allows a great deal of flexibility in design as well as application.

1.3.1 Space Applications

Shape memory alloys possess many attributes which make them extremely favorable for space-based applications. Compared to devices such as wax actuators and thermostatic elements, SMA's have a significantly higher force output-to-weight ratio [Ohkata & Suzuki 1998]. This is an important advantage bearing in mind the premium costs per pound to put a spacecraft in orbit. Their high reliability and long fatigue life are favorable attributes for the long-term, autonomous operation required of spacecraft systems. Their ability to act as both sensor and actuator means simplicity of design and operation, and fewer components that could be susceptible to failure than their more complicated counterparts. Their ability to be drawn into wire or fabricated into a variety of shapes allows great flexibility in design, and their operation produces no risk of

sparking or debris contamination. Additionally, they possess a high stroke length-to-weight ratio, which adds to their feasibility as actuator elements.

SMA-based devices have found practical applications in large deployable space structure designs, both as deployment mechanisms and for vibration damping [Schetky 1990]. Further applications include latching mechanisms, fail-safe actuators, isolation valves, and cable release mechanisms [TiNi Aerospace Inc.]. Concepts for shape-memory based solar panel release mechanisms have also been explored [Voggenreiter *et al*. 1999]. A particular advantage to their use as deployment mechanisms is their ability to move with slow, controllable motions, thus minimizing inertial shocks to the structure during deployment or actuation. SMA devices have been flight tested and proven in service on such missions as the Clementine mission for lunar exploration and the Mars Global Surveyor spacecraft [TiNi Aerospace Inc].

SMA thermal conduction switches such as the one described in this thesis could easily be employed for spacecraft thermal control. Onboard electronics produce heat that must be dissipated in order to keep the electrical systems within their operational temperature ranges. Dissipation of heat to a space radiator eliminates this problem, but is often accomplished through an active control, such as a pump [McMordie and Panetti 1999]. An SMA-based conduction switch could provide a direct conductive path to a space radiator in a passive, autonomous manner, which would eliminate the need for the pump.

1.4 Continuing Work

The work described in this thesis represents the ongoing effort to design a thermal conduction switch as described in section 1.1 in response to NASA-KSC's mandate for

cryogenic thermal management. This work presents the characterization of the Ni-Ti-Fe alloy, particularly with respect to its unique low-hysteresis attributes. The characterization method of dilatometry is explored in some detail, including commissioning of a liquid helium differential dilatometer. Further, this work includes testing of the Ni-Ti-Fe alloy in a previously designed switch configuration to verify its feasibility as a low-hysteresis actuator material. A design concept for a conduction switch that minimizes the thermal gradient is also discussed.

CHAPTER TWO: LITERATURE REVIEW

An equiatomic alloy of nickel-titanium is among the most commonly used in industry and in particular for actuator applications, owing to their pronounced shape memory effect. The hysteresis associated with these alloys, however, is typically in the range of 40 °C [Saburi 1998]. Development of a low-hysteresis thermal actuator requires an alloy that has both low hysteresis and exhibits the shape memory effect. This requirement can be met with Ni-Ti-Fe alloys due to their characteristic R-phase transformation, which is discussed in further detail in the following sections.

2.1 The R-Phase

As previously discussed, most shape memory alloys undergo a phase transformation from martensitic (monoclinic crystal lattice) to austenitic (body-centered cubic lattice). However, an intermediary phase change exists in certain alloys that is rhombohedral in nature, and occurs between the M_s and A_s transformation temperatures. It can be brought about in shape memory alloys by increasing nickel content, ageing after solution treatment, cold working followed by annealing at temperatures below recrystallization, thermal cycling, or substitution of a third element, such as iron or aluminum, for nickel [Miyazaki & Otsuka 1986]. While the shape memory effect associated with the martensite → austenite phase transformation is typically in the 8% range, the SME associated with the R-phase transformation exhibits a much smaller shape change—typically 1% or less [Uchil 2002]. The temperature hysteresis associated with the R-phase, however, is also notably smaller—on the order of 10 °C down to one or two °C—compared to the 40 °C hysteresis typical of the martensitic phase change. Actuators designed to

operate within the R-phase transformation temperature range have, as another advantage, a high fatigue life, owing to the small 1% strain.

The R-phase transformation, before it was well understood, was first observed as a 'premartensitic' phenomenon such as a rise in electrical resistivity, electron diffraction pattern streaks, extra spots at the 1/3 positions in both X-ray and electron diffraction patterns, a decrease in sound velocity, a decrease in elastic modulus, and specific heat peaks [Hwang *et al.* 1983]. Hwang *et al*. [1984] observed evidence of the R-phase in a $Ti_{50}Ni_{47}Fe_3$ in the form of near-1/3 superlattice reflections in electron diffraction patterns that intensified with a temperature decrease between 0 °C and -10 °C. The group noted that the appearance and disappearance of these near-1/3 reflections were both temperature-dependent and thermally reversible without hysteresis. At lower temperatures, the near-1/3 reflections were found to lock solidly into the exact 1/3 positions. Using TEM, Hwang *et al*. found further evidence of the phase change by correlating the appearance of antiphase domains in the sample over the same temperature range. Through their electron diffraction pattern observations, the group was able to confirm the rhombohedral structure of the R-phase by noting the elongation of the parent phase CsCl crystal structure along the <111> body diagonals during the austenite → R-phase change. They classified this phase change as a first-order transformation, due to the sudden onset of the rhombohedral angle (89.3° from 90°) rather than a gradual decrease in angle.

2.1.1 Cycling Effects on the R-Phase

In order to establish the feasibility of utilizing the R-phase for actuator design, it is important to verify the stability of the alloy's properties during thermomechanical cycling.

Tobushi *et al*. [1996] investigated the effects of cycling on the shape memory effect and superelasticity of a NiTi sample in the R-phase region. The alloy was strained repeatedly to a maximum of 1%, unloaded, and heated to allow shape recovery. The stress-strain behavior and shape recovery trends over 10 cycles are shown in Figure 2.1 below. They show little variance with the number of cycles, and therefore a definitive stability due to cyclic deformation. When the sample is repeatedly strained up to 6%, however, the reverse transformation temperature increases with the number of cycles due to an accumulation of dislocations (and therefore internal stresses) [Tobushi *et al*. 1996].

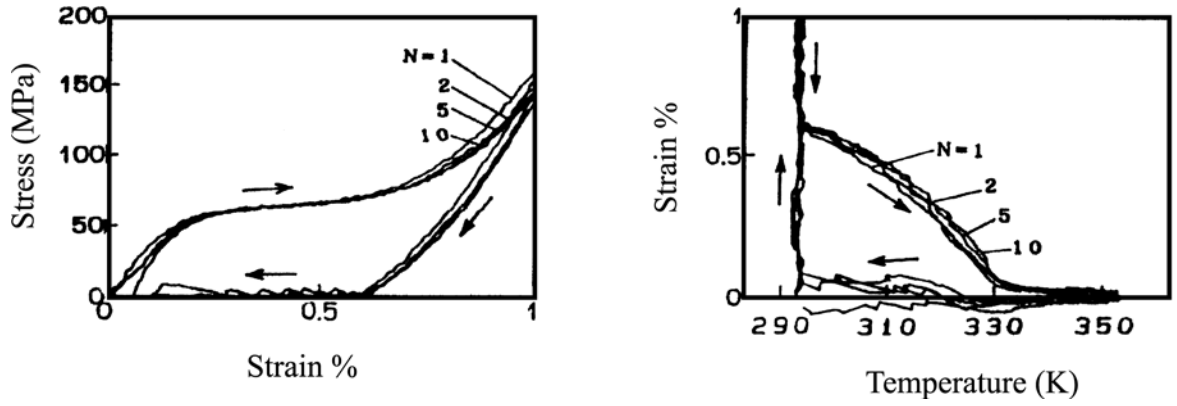

Figure 2.1: Stress-strain and strain-temperature relationships for thermomechanically cycled NiTi [Tobushi *et al*. 1996].

When the stress-strain cycling is repeated at a constant temperature above A_f at strains of up to 1%, the resulting stress-strain curves show very little change over 20 cycles, and a small hysteresis between the loading and unloading curves which is less than 20 MPa [Tobushi *et al*. 1996]. These results suggest cyclical stability for superelasticity associated with the R-phase transition [Tobushi *et al*. 1996].

2.1.2 Effect of Thermomechanical Treatments on the R-Phase

The R-phase can be induced in binary NiTi alloys by means of thermomechanical treatments, consisting of any combination of solutionizing, ageing, cold working followed by annealing, and thermal cycling [Miyazaki & Otsuka 1986]. Binary NiTi alloys which are slightly nickel-rich tend to be more susceptible to solutionizing treatments, which have the effect of producing Ti_3Ni_4 precipitates in the matrix [Jinfang *et al*. 1992]. These precipitates produce strain fields in the B2 parent matrix, which effectively strengthens the matrix and aids in the improvement of the overall shape memory effect [Saburi 1998]. Further, thermomechanical treatment of near-equiatomic NiTi alloys can induce the R-phase, as explored by Jifang *et al*. [1992]. The group investigated the effects of cold working at different rates, followed immediately by annealing at different temperatures. Figure 2.2 shows the results of cold working rate on the transformation temperatures of near-equiatomic NiTi alloys.

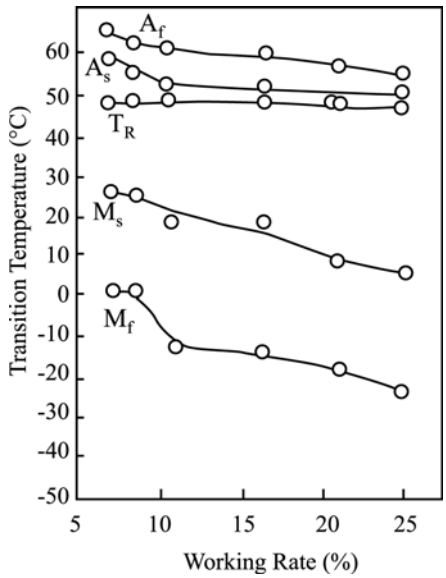

Figure 2.2: Influence of cold working rate on transition temperatures of near-equiatomic NiTi. (Samples were annealed at 500 °C for 1 hour following cold work.) [Jinfang *et al*. 1992].

As seen from the figure, the transition temperature of the R-phase changed very little with the amount of cold working. However, the martensitic transformation temperatures decreased noticeably as the cold working rate increased, thus enlarging the temperature range over which the R-phase is stable. The shape memory effect showed a noticeable improvement with the increase in cold working rate, and can be correlated to an increase in R-phase stability range [Jinfang *et al*. 1992]. The results found by Jinfang *et al*. substantiates earlier work by Miyazaki and Otsuka which showed that the dislocations produced by cold working and the precipitates produced by solution treatment both served to introduce back stresses around them in the material. The back stresses, which are amplified by the magnitude of the strain caused by the phase change, cause the martensitic transformation to be suppressed to a lower temperature [Miyazaki & Otsuka 1986]. The increase in internal stresses is also responsible for widening the distance between the M_s and M_f temperatures [Miyazaki & Otsuka 1986]. It has also been demonstrated that dislocations are more effective than precipitates in increasing the critical stress required to move interface boundaries, both in martensite and the R-phase [Miyazaki & Otsuka 1986].

Annealing temperature can also have a profound effect on the R-phase and the shape memory properties of NiTi alloys. For a near-equiatomic NiTi alloy cold worked at 22.3%, annealing at 400 °C for one hour showed the best recovery rate, the best superelasticity, and the greatest R-phase stability [Jinfang *et al*. 1992]. As annealing temperature increases, however, several things occur: the distance between the R-phase transition temperature and the martensitic transformation temperature narrows, and eventually disappears at 600 °C, the dislocation density decreases, and eventually recrystallization at 600 °C occurs [Jinfang *et al*. 1992]. As the

annealing temperature is increased, the shape memory recovery decreases slightly, and decreases significantly at 600 °C when the R-phase disappears [Jinfang *et al*. 1992].

Thermal cycling can also be a factor in revealing the R-phase. Repeated thermal cycling can introduce dislocations into the material due to strains associated with the forward and reverse transformations. Thermal cycling has been shown to depress the M_s temperature only slightly, however, allowing only a very narrow temperature range over which the R-phase is stable [Miyazaki & Otsuka 1986].

2.2 Characteristics of Ni-Ti-Fe Alloys

The transformation temperatures of shape memory alloys are extremely affected by the chemical composition of the alloy on the order of 1 at% changing the M_s temperature by as much as 100 °C [Otsuka & Ren 2002]. The substitution of a small percentage of iron for nickel in NiTi based alloys has the effect of lowering the martensitic transformation temperature M_s, as well as increasing the temperature range between the R-phase → martensite and the austenite → R-phase transformations [Saburi, 1998]. As the percentage of iron increases, the R-phase transformation temperature shows a gradual decrease, but the addition has a much more pronounced effect on the martensitic transformation [Canales *et al*. 1995]. Depression of the M_s temperature is ascribed to a difference in free energy changes between the R-phase and the martensite phase induced by addition of the third element [Miyazaki & Otsuka 1986]. This combination of characteristics is favorable for an actuator design that makes use of the R-phase transformation at cryogenic temperatures.

2.2.1 Ni-Ti-Fe Phase Changes

Separation of the R-phase from the martensite phase makes it possible to more readily observe the distinctly different properties of the R-phase and the martensite phase. The substitution of 3% iron for nickel in NiTi lowers the M_s temperature by more than 100 °C [Hwang & Wayman 1983, Jiménez *et al*. 1991]. For this reason, Hwang *et al*. chose the $Ti_{50}Ni_{47}Fe_3$ alloy for study of the transformation behavior. Hwang *et al*. [1983] observed the appearance of 'needle-like' domains in this alloy associated with the formation of the R-phase, and noted a small hysteresis with the appearance and disappearance of these domains. This hysteresis further confirmed the first-order transformation [Hwang *et al*. 1983]. Using electron diffraction, the group confirmed the rhombohedral crystal structure of the R-phase and noted that the 'needle-like' domains had differently-oriented rhombohedral structures, or twinned variants. These twins are formed in a similar manner as in the austenite → martensite phase transformation described in Chapter 1, in order to accommodate the strains associated with the rhombohedral lattice distortion [Hwang *et al*. 1983]. A study of the $Ti_{50.1}Ni_{46.7}Fe_{3.2}$ by the same group indicated similar trends, with the onset of the R-phase transition occurring at about –49 °C.

Study of the martensitic transformation of TiNiFe by Hwang *et al.* was limited to the $Ti_{50}Ni_{47}Fe_3$ alloy, since it has a higher transformation temperature than $Ti_{50.1}Ni_{46.7}Fe_{3.2}$. The group found the M_s temperature to be about –98 °C, at which point they observed the formation of lenticular plates of twinned martensite. Goo *et al*. [1985], however, reported the martensitic start temperature of the same alloy to be -140 °C. Electron diffraction patterns of the $Ti_{50}Ni_{47}Fe_3$ sample obtained while the material was martensitic confirmed the hypothesis that the crystal structure was a distorted orthorhombic (monoclinic) crystal structure [Hwang *et al*. 1983]. The

group concluded that the sequence of phase changes in the $Ti_{50}Ni_{47}Fe_3$ alloy proceeds as follows: austenite (B2 structure) → incommensurate phase (distorted cubic) → commensurate phase (rhombohedral) → martensitic phase (monoclinic B19' structure) [Hwang *et al*. 1983, 1984]. The B2 → incommensurate phase is a second order transition which results in an incommensurate superlattice, and the following incommensurate → commensurate phase change is a first order transition that involves the transition of a distorted CsCl lattice into a rhombohedral structure [Hwang & Wayman 1983]. It is common, however, for both the incommensurate and the commensurate phase changes to be referred to as "intermediate phase" without distinguishing between them [Honma 1984].

Figure 2.3 shows the presence of the R-phase in the $Ti_{50}Ni_{47}Fe_3$ alloy as seen by variations in the electrical resistance. Note that the hysteresis associated with the martensitic

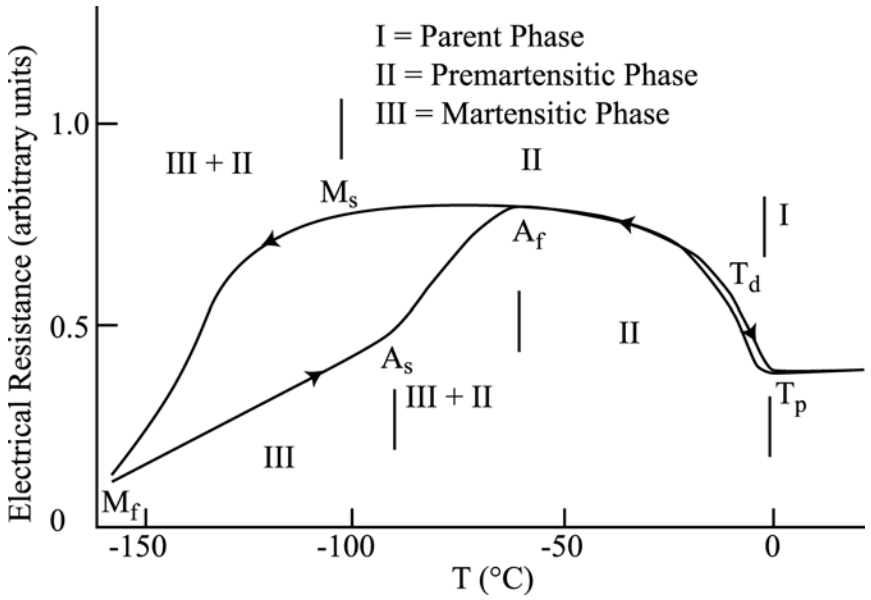

Figure 2.3: Electrical resistance as a function of temperature for $Ti_{50}Ni_{47}Fe_3$ alloy [Hwang *et al*. 1983].

transformation is about 20 °C, and the much smaller hysteresis related to the reverse transformation from the R-phase to the austenite phase. Nearly identical results were found by Honma *et al*. [1984] in the same alloy during an electrical resistivity test, who noted that the I ↔ II transition was almost completely reversible.

The martensitic transformation temperature, as mentioned previously, is drastically reduced by the addition of iron to the binary NiTi system. In some alloys it is possible to completely suppress the martensitic transformation. Canales *et al*. [1995] performed resistivity measurements on a sample of $Ti_{50}Ni_{45}Fe_5$ from room temperature down to 4 K and found no evidence of martensitic transformation.

2.2.2. Mechanical Properties of Ni-Ti-Fe

Ren *et al*. [2001] conducted a comparative study of the elastic constants of Ti-Ni-based alloys, and found that substituting a small amount of iron (2 at%) for nickel had no effect on the value of the elastic constant at the rhombohedral start (R_s) temperature. In this study, the elastic constant refers to the stiffness in the <110> direction [Otsuka and Ren 2002]. Figure 2.4 illustrates this concept.

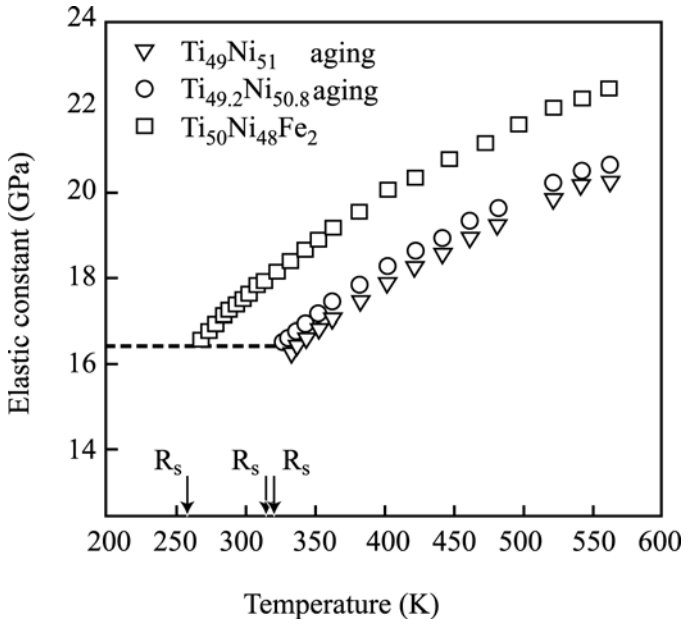

Figure 2.4: Temperature dependence of the elastic constant (stiffness in the <110> direction) for three different Ti-Ni-based alloys [Ren *et al*. 2001].

The figure shows that addition of iron makes the material harder (i.e. an increase in elastic constant). In order for the elastic constant to remain the same, the transformation temperature must be lower [Otsuka & Ren 2002].

Jiang and Xu conducted a series of tests to correlate stress-strain behavior of different Ni-Ti-Fe compositions with temperature. Figure 2.5(a) shows the stress-strain behavior of four different alloy compositions at room temperature. Before testing, the alloys were annealed for 1 hour at 800 °C and water quenched. The trends show marked differences because $Ti_{50}Ni_{48.5}Fe1.5$ and $Ti_{50}Ni_{48}Fe_2$ contain both martensite and austenite at room temperature, and the other two alloys are completely austenitic [Jiang & Xu 2000]. Note the higher yield strength of the two compositions containing the highest amounts of iron. Figure 2.5(b) shows the same four alloy compositions at –70 °C. At this temperature, the alloys are martensitic, and show three different

regions: elastic deformation of martensite, reorientation of martensite variants (detwinning), and ductile deformation of martensite [Xu *et al*. 2000].

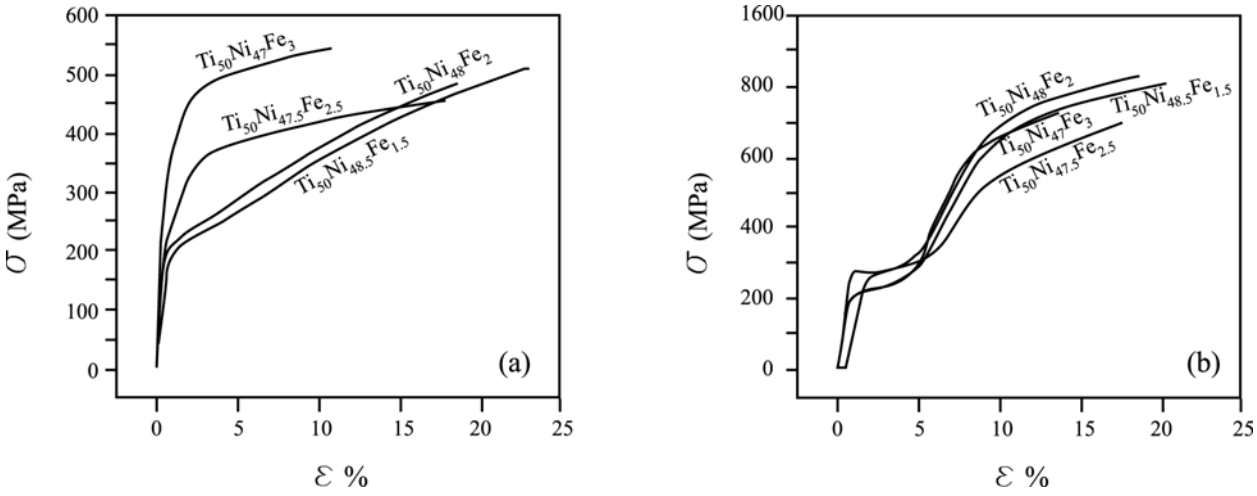

Figure 2.5: Stress-strain curves of various alloys (a) at room temperature, and (b) at –70 °C [Jiang & Xu 2000].

A similar stress-strain curve for a $Ti_{50}Ni_{47.5}Fe_{2.5}$ alloy (Figure 2.6) was obtained by Saburi, which shows the same type two-step deformation regions as in Figure 2.5(b). This alloy, although chemically identical to the sample in Figure 2.5(b), was annealed at 500 °C for 1 hour after cold-rolling 30%. The test was conducted at –80 °C when the alloy was completely in the R-phase. The first small slip region (about 0.8%) can be attributed to reorientation of the R-phase variants (detwinning), and the second, larger slip region to formation of stress-induced martensite [Saburi 1998]. The 1% residual strain after unloading was recovered after heating the sample and allowing it to return to the austenite phase. The differences between Figure 2.5(b)

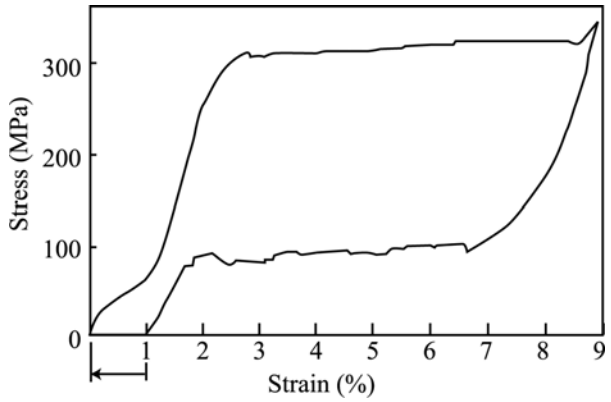

Figure 2.6: Stress-strain curve for a $Ti_{50}Ni_{47.5}Fe_{2.5}$ alloy tested at –80 °C [Saburi 1998].

and Figure 2.6 may be attributed to the cold-rolling in Saburi's sample. The higher dislocation density would act to stabilize the martensite, allowing the formation of stress-induced martensite to occur more readily.

Jiang and Xu studied the shape memory effect in several Ni-Ti-Fe alloys at –70 °C, and found the composition $Ti_{50}Ni_{47}Fe_3$ to have the highest strain recovery rate (93.5%) for an 8% strain. Further investigation of this alloy revealed 100% recovery up to the 8% strain with a decrease in recovery at strains of 8% and higher. Their results are summarized in Table 2.1 below.

Table 2.1: Shape memory effects of the $Ti_{50}Ni_{47}Fe_3$ alloy at –70 °C [Jiang & Xu 2002].

Deformation (%)	**Residual deformation %**	**Permanent deformation %**	**Shape memory strain %**	**Recovery %**
4	2.19	0	2.19	100
6	3.59	0	3.59	100
8	6.2	0.4	5.80	93.5
10	7.49	1.99	5.50	73.4

Similar testing was conducted on a $Ti_{50}Ni_{48}Fe_2$ alloy at −70 °C to determine the alloy's shape memory characteristics. The maximum shape memory strain (5.6%) was observed at 8% deformation [Xu *et al*. 2000]. When deformed in the austenitic state, the $Ti_{50}Ni_{48}Fe_2$ alloy exhibited the maximum shape memory strain (4%) at 10% deformation [Xu *et al*. 2000].

2.2.3 Twinning in Ni-Ti-Fe

Goo *et al*. [1985] investigated the phenomenon of twinning in a Ni-Ti-Fe alloy for the purpose of understanding mechanical twinning vs. pseudo-twinning. Psuedo-twinning is defined as the configuration of a crystal when the atomic lattice sites are in a twinned orientation, but the atomic ordering is destroyed [Goo et al. 1985]. In mechanical twinning, as described in Chapter 1, the atomic sites are in a twinned orientation and the crystal remains ordered. In BCC metals, a simple shear can result in mechanical twinning. In the B2 (CsCl) structure, however, the shear alone produces pseudo-twinning, since the ordering of the atoms is changed. A slight "shuffle" of the atoms must accommodate the shear in order to maintain the stable B2 structure [Goo *et al*. 1985].

2.3 Thermomechanical Processing

There are several factors which can affect the transformation temperatures of shape memory alloys, and these must be taken into account with design of a temperature-controlled actuator. The introduction of dislocations into the material effectively lowers the martensitic transformation temperature [Otsuka & Ren 2002]. As an actuator is repeatedly cycled, the dislocation density increases and M_s will show a decrease [Otsuka & Ren 2002]. The addition of

dislocations can also affect the stress at which stress-induced martensite begins to form. The dislocations can act as favorable nucleation sites, allowing martensite to form more readily with the addition of a lower critical stress [Otsuka & Ren 2002].

Introduction of dislocations can also affect the reverse transformation, as investigated by Jiang and Xu. They found, using differential scanning calorimetry on samples of NiTi with different strains, that as the strain increased, the A_s temperature increased and A_f temperature moved closer to A_s. This showed that the reverse martensitic transformation was occurring more quickly in samples with higher dislocation densities [Jiang & Xu 2002]. The resulting correlation between strain and transformation temperatures is summarized in Table 2.2.

Table 2.2: Reverse transformation temperature variation with strain [Jiang & Xu 2002].

Strain (%)	A_s (°C)	A_f (°C)	Latent heat (w/g)
0	56	68	20.00
2	65	78	20.03
4	72	80	19.28
6	86	92	19.84
8	93	98	19.56
10	98	102	21.25
12	104	108	21.16

Jiang and Xu found that the increase in peak temperature was linear up to 8% deformation, at which point it showed a more rapid increase. They also found that the latent heat associated with the transformation remained fairly constant until the 8% strain was exceeded, at which point the latent heat increased slightly. The increase in transformation temperature has been explained as follows: the dislocations serve to stabilize the martensite by introducing a single martensite variant and lowering its free energy, making it more difficult for the reverse

transformation to austenite to take place [Xu *et al*. 2000, Jiang & Xu 2002]. At strains higher than 8%, plastic deformation and permanent damage to the lattice structure occurs, leading to a more rapid increase in transformation temperature [Jiang & Xu 2002].

Yield strength and ductility are also affected by cold working and annealing. Cold working introduces a combination of dislocations and twins into the material structure. The spacing between the twins decreases with increasing amount of cold working [Moberly *et al*. 1990]. The annealing process causes subgrains to form preferentially at the twinned locations [Moberly *et al*. 1990]. Therefore the subgrains produced in a heavily cold worked material are small and refined, which creates a good combination of strength and ductility [Moberly *et al*. 1990]. Moberly *et al*. investigated several $Ti_{50}Ni_{47}Fe_3$ samples with different combinations of cold working and annealing. Unlike cold working NiTi alloys, which causes the formation of stress-induced martensite, this does not happen with $Ti_{50}Ni_{47}Fe_3$ since the martensitic transformation temperature is repressed to well below room temperature [Moberly *et al*. 1990]. The results are summarized in the table below:

Table 2.3: Mechanical properties of worked and annealed $Ti_{50}Ni_{47}Fe_3$ [Moberly *et al.* 1990].

Work Condition	**Heat Treatment**	**Yield strength (MPa)**	**Elongation at failure (%)**
Fully annealed	2 hr at 875 °C	410	30-50
10% cold swage	No heat treatment	690	13
10%	10 min at 400 °C	650	26
10%	10 min at 450 °C	560	25
10%	1 min at 500 °C	555	32
10%	10 min at 500 °C	510	26

Work Condition	Heat Treatment	Yield strength (MPa)	Elongation at failure (%)
10%	100 min at 500 °C	500	30
30% cold swage	No heat treatment	1030	7
30%	10 min at 350 °C	840	17
30%	10 min at 400 °C	800	13
30%	10 min at 450 °C	750	20
30%	1 min at 500 °C	740	25
30%	10 min at 500 °C	700	22
30%	100 min at 500 °C	660	25
30%	1000 min at 500 °C	640	30
30%	10 min at 550 °C	630	31
30%	10 min at 600 °C	580	31
40% cold swage	No heat treatment	1090	4
40%	10 min at 400 °C	850	29
40%	10 min at 500 °C	730	24

For an actuator application, both strength and ductility are important factors. Table 2.3 shows an increase in yield strength with an increase in the amount of cold working. Annealing the cold worked alloys decreases the yield strength, but increases ductility. The sample with the best combination of strength and ductility was cold worked at 40% and annealed for 10 minutes at 400 °C.

CHAPTER THREE: NI-TI-FE CHARACTERIZATION

Characterization of Ni-Ti-Fe alloys requires the ability to measure phase transition temperatures in the cryogenic range. While the R-phase transition temperature typically occurs within the range of liquid nitrogen temperatures (above 77 K), the martensitic transition temperatures are often well below this temperature. In order to fully characterize the phase transition temperatures of Ni-Ti-Fe, therefore, it is necessary to have the means to test the material at lower temperatures. A custom liquid helium differential dilatometer purchased from Theta Industries was commissioned by the author to meet this need. It provides the ability to determine phase transition temperatures down to a temperature of 20 K. This chapter includes a description of differential dilatometry, a detailed description of the system components, and operational instructions. It also includes an introduction to differential scanning calorimetry.

3.1 Differential Dilatometry

A dilatometer measures the expansion and contraction of a sample corresponding to changes in temperature. The expansion and contraction is detected by a sensitive linear variable differential transformer (LVDT) connected to a pushrod, which holds the sample in place. Figure 3.1 shows a schematic of the sample and reference setup. As the sample expands (or contracts), it pushes against the core pushrod, which in turn moves the LVDT core through a coil and generates an associated voltage. The reference, which is a material with a known expansion rate, expands or contracts against the coil pushrod. The coil and core are connected by frictionless springs, which allow them to move along a common axis. The position of the coil and core in

relation to each other generates a particular voltage, which can be interpreted as linear expansion or contraction of the specimen material.

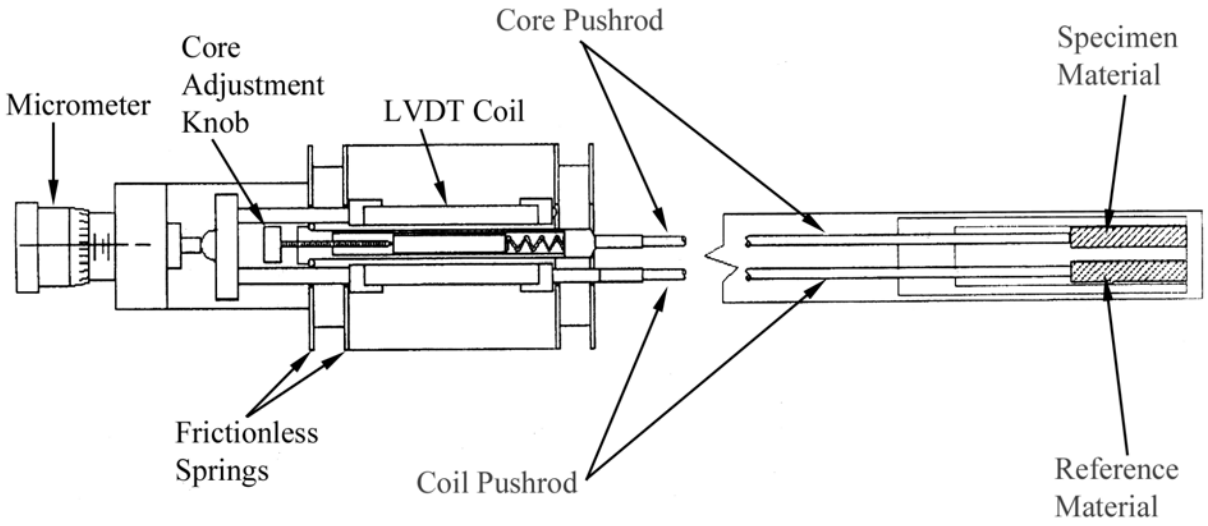

Figure 3.1: Differential sensor reference and specimen setup [Theta Industries, Inc.].

The data obtained from the LVDT output can be used to create graphs of sample expansion vs. temperature and to calculate the coefficient of thermal expansion vs. temperature for a material. In the case of Ni-Ti-Fe characterization for actuator applications, pinpointing phase transformation temperatures in the cryogenic range is the primary goal of the dilatometric study. A phase transformation is observed as a sudden, non-linear region in the expansion vs. temperature plot. This occurs due to the shape and/or volumetric change of the crystal structure during a phase change, such as a body-centered cubic structure transforming to a rhombohedral structure.

3.1.1 Commissioning of the Liquid Helium Differential Dilatometer

The liquid helium differential dilatometer main system components are shown in Figure 3.2.

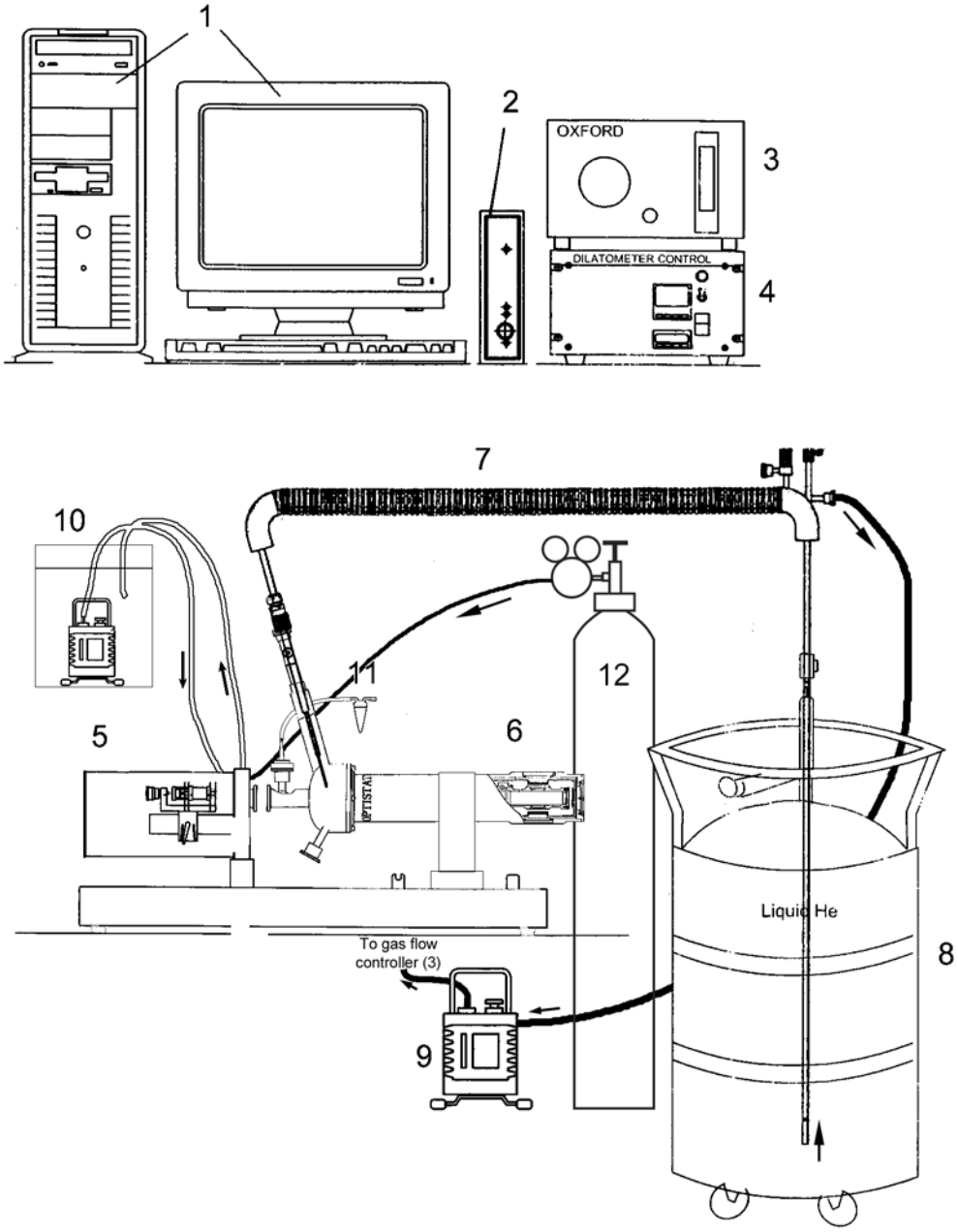

Figure 3.2: Liquid helium differential dilatometer major system components.

During testing, the liquid helium is drawn from the liquid helium dewar (8) up through the central core of the low-loss helium transfer tube (7), and into the heat exchanger of the cryostat (6). Liquid helium is difficult to maintain in liquid form due to the small amount of latent heat required to cause boiling. Transferring it from the dewar through the transfer tube and into the cryostat while maintaining it in the liquid phase therefore requires extra care and provision to prevent heat influx, particularly in the engineering of the transfer tube. The helium is drawn through the central core of the transfer tube, which is concentrically shielded by a layer of cold helium gas. That layer, in turn, is vacuum shielded from the outer layer of the tube. As the liquid helium circulates through the heat exchanger, it boils and the cold gas is drawn back out of the cryostat by the vacuum pump (9) through the cold gas layer of the transfer tube, and into the helium gas flow meter (3). The gas flow meter contains a float gauge to measure the volume of helium, which is then vented out a port on the back of the flow meter (3).

The cryostat is connected to an LVDT (5), which was discussed in section 3.1. The voltage signal from the LVDT goes through the signal conditioner (2) and back to the computer running DilaSoft software (1). Since temperature fluctuations in the surrounding environment can affect the precision of the LVDT, it is surrounded by a double-walled, vacuum tight box. The box has an inlet and outlet to allow circulation of temperature-controlled water (10) between the walls, which helps to maintain a constant temperature environment for the LVDT inside.

Between the LVDT and the specimen tube is the measuring head, which contains wiring for the specimen thermocouple, an electrical port to the signal conditioner, an inlet port for the shielding gas, and ports for the water circulation system. The shielding gas (12), or exchange gas, is a high-purity helium gas that flows in through the measuring head and into the sample chamber. The exchange gas serves two purposes: it provides efficient heat transfer between the

sample and the heat exchanger, and it prevents frost from forming in the sample chamber during cryogenic tests. Flow of the exchange gas through the sample chamber is monitored by the gas bubbler (11).

Temperature is monitored and controlled by the temperature controller (4). The controller monitors the cryostat temperature sensor, and controls the setpoint temperature of the furnace during heating. The setpoint is part of the temperature program calculated by the software to produce a constant heating rate. The cooling rate is controlled only by increasing or decreasing the flow of liquid helium through the cryostat.

The internal structure of the cryostat contains several layers, as shown in Figure 3.3. The innermost chamber is the cylindrical sample space, into which the hollow glass specimen holder containing the sample and reference material is placed. The structure surrounding the sample chamber contains the heat exchanger, which cools the sample space without being in direct physical contact with the sample. The liquid helium flows through the cryostat's heat exchanger where it boils off and is drawn back out through the transfer tube. The heat exchanger is surrounded by an aluminum radiation shield. Between the radiation shield and the outer layer is the outer vacuum chamber, which provides thermal isolation for the heat exchanger and internal components from the outer environment. The outer vacuum chamber is evacuated through the vacuum port shown in Figure 3.3.

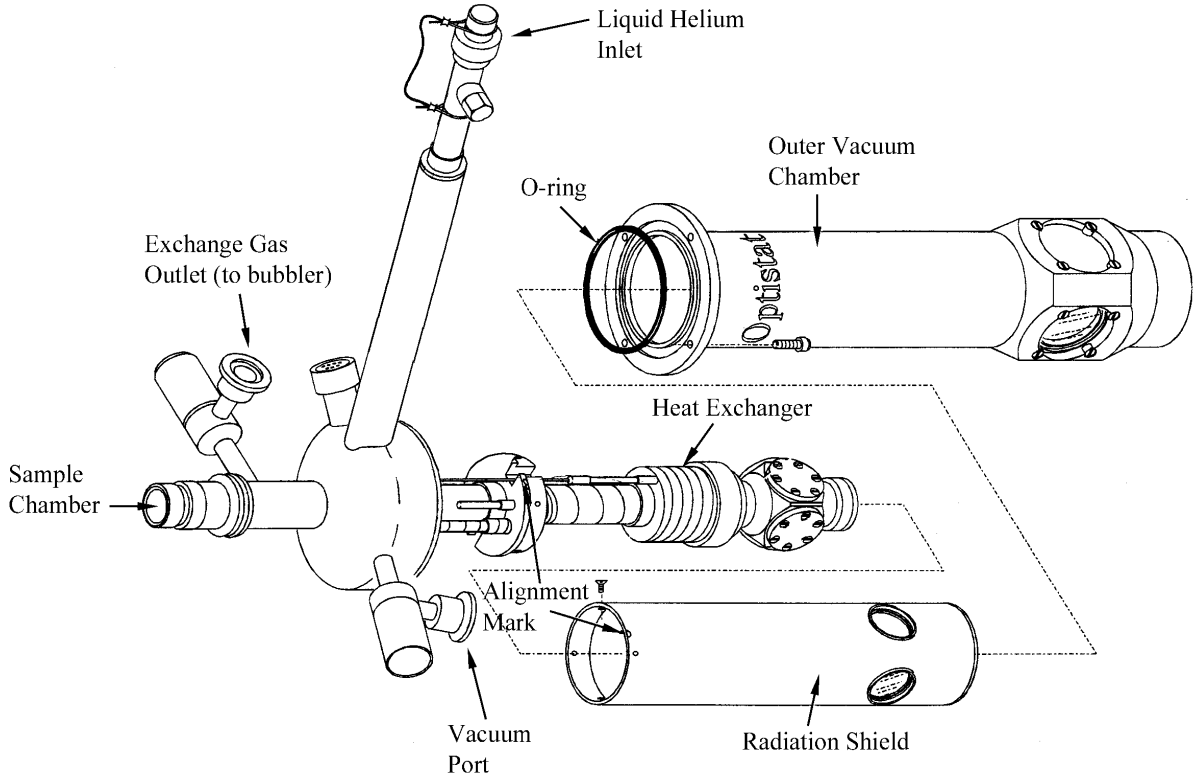

Figure 3.3: Cryostat assembly [Oxford Instruments 2003].

3.1.2 Dilatometer Operating Instructions

Note: This section includes the complete operating procedures for running an experiment using the Dilatronic VIII Liquid Helium Dilatometer. Additional information regarding maintenance procedures, proper installation methods and troubleshooting can be found in the Oxford Instruments Operator's Handbook, the Theta Industries Manual and the DilaSoft Help File.

WARNING: IMPROPER HANDLING OF CRYOGENS CAN CAUSE SERIOUS INJURY. WEAR PROPER SAFETY PROTECTION ON EYES AND EXPOSED SKIN DURING ALL PROCEDURES INVOLVING CRYOGEN HANDLING.

WARNING: MAKE SURE THE WORK AREA IS WELL VENTILATED. HELIUM DISPLACES OXYGEN, WHICH CAN LEAD TO ASPHYXIATION.

CAUTION: DO NOT OPEN ANY VALVES ON THE DEWAR IF THE PRESSURE GAUGE READS BELOW ZERO. AN INFLUX OF AIR WILL CAUSE ICE TO FORM INSIDE THE DEWAR, WHICH CAN BLOCK THE VENT VALVES AND LEAD TO AN OVERPRESSURIZATION CONDITION.

3.1.2.1 Experiment Preparation and Loading

1. Make sure the calibration is up to date by clicking on the Calibration tab. If the calibration is up to date, perform a calibration check (see the "Check Calibration" section below).
2. If temperature fluctuations in the operating environment are significant (more than 2 °C), use the water circulator. Allow the water circulator to run for at least 2 hours prior to the test run. Recommended water temperature is 30-40 °C. If ambient temperature fluctuations are not expected to vary during the test, using the water circulator is not necessary.

3. Slide the cryostat back to reveal the sample holder and push rods.
4. Make sure reference material and sample have been accurately measured with high quality calipers. The length of the sample should be the same length as the reference.
5. Check to make sure that the LVDT retaining spring is not installed, and ensure that the push rods are aligned properly and not touching each other or the specimen holder. The push rods should be slightly suspended above the specimen platform, and the specimen thermocouple should be positioned under the specimen platform.
6. Make sure the power controller is turned on (but not the furnace). In the DilaSoft software, click on the "Check Calibration" button. Press "OK" when the message box appears. A Calibration Check screen will then appear with a position meter. This shows the position of the push rods (positive position change for the sample rod and negative position change for the reference rod). *Note: A calibration check is not being performed at this time. The software's position meter is only being used to aid in proper LVDT placement*.
7. Thoroughly clean the reference and sample materials. Carefully place the sample onto the specimen platform so that it is aligned with the core push rod and its back end is pushed up against the end of the specimen tube. Carefully move the LVDT forward so that the push rod is just touching the sample, but not applying any force. Note the position reading from the software.
8. Slowly and carefully, move the LVDT forward toward the sample until the software shows a positive displacement of 1 mm (The difference between the position noted in step 7 and the new position should be 1 mm). Lock the LVDT into place. *Note: If*

significant expansion of the sample is expected during the experiment, the displacement difference should be reduced to about 0.5 mm.

9. Place the reference onto the front push rod in the same manner as the sample. The force from the push rods should hold both the reference and the sample securely in place for the duration of the experiment. *Note: Choice of sample material should be based on the temperature range over which the experiment will be run. The lower temperature boundary for the copper reference is -253 °C; the lower boundary for fused silica is -193 °C. During execution of the program, if the sample temperature exceeds the upper or lower limits of the reference being used, the temperature program will automatically terminate. If the temperature program will exceed the limit, define the reference material on the Main menu as "unknown" (See "Setting the Experiment Parameters" section below).*
10. Make certain that the sides of both the sample and the reference are parallel and not touching each other or the sides of the specimen tube.
11. Lightly tap the bottom side of the end of the specimen tube to set the position of the sample and reference materials, so that they will not shift once the test has begun. Wait for the position reading to stabilize and note the final position reported by the software.
12. Close the measuring head cover and secure it with the two nuts. Slowly and carefully slide the cryostat over the specimen tube and secure it with the vacuum clamp.
13. Check the position reading reported by the software. If it has changed significantly, slide the cryostat open again and check the positioning of the sample and reference.

14. After the sample and reference positioning has been verified and the cryostat and measuring head cover have been closed, push the “cancel” button on the calibration check screen to return to the main software interface.
15. If the water circulator is being used, allow the system to sit until the temperature is sufficiently stabilized.
16. Set the temperature program and program parameters (See the “Writing the Temperature Program” and “Setting the Experiment Parameters” sections below).
17. With the bubbler disconnected, start the He gas flow through the specimen area. Use a high flow rate initially, and then change it to about 5 cc/min for the duration of the test. If a flow meter is not available, reduce the helium flow after the initial high-flow purge, and connect the bubbler to the sample chamber outlet port on the cryostat. Adjust the flow regulator on the helium gas cylinder until one bubble appears approximately every 15 seconds. The slower the helium gas flow rate, the more quickly the sample space will cool.

    CAUTION: DO NOT TURN OFF THE HELIUM FLOW COMPLETELY. COMPRESSION OF THE HELIUM GAS INSIDE THE SAMPLE SPACE DUE TO REDUCED TEMPERATURES WILL CAUSE THE OIL FROM THE BUBBLER TO BE DRAWN BACK DOWN THE TUBE INTO THE SAMPLE SPACE. MONITOR THIS CAREFULLY!

3.1.2.2 LVDT Calibration

The calibration check should be done at least once a week, or preferably before each experiment. A full calibration should be done every 30 days. The due date for the next full calibration is displayed on the Calibration screen.

3.1.2.2.1 Check Calibration

1. From the DilaSoft main screen, click on the Calibration tab.
2. Make sure the power controller is turned on (but not the furnace).
3. Load the sample (but not the reference) as described in the "Experiment Preparation and Loading" section.
4. Click on the Check Calibration button at the bottom of the window. Press "OK" when the message box appears. A Calibration Check screen will appear with a position meter.
5. Slide back the measuring head cover to reveal the LVDT. Turn the micrometer until it is close to touching the ball at the end of the LVDT, and install the retaining clip.
6. Turn the micrometer until the software position meter shows a reading of zero (or as close as possible). Then turn the micrometer again to the nearest whole number division marker towards the positive direction. Wait for the reading on the software to stabilize, and press the "Take Reading" button.
7. Turn the micrometer exactly one full turn in the positive direction (clockwise looking in the direction from the micrometer towards the cryostat). Wait for the reading on the software to stabilize and press the "Take Reading" button.

8. Turn the micrometer exactly one full turn in the negative direction (counter-clockwise). Go slightly past the starting point number, and then back to it. Wait for the reading to stabilize and press “Take Reading”.
9. Turn the micrometer one full turn in the positive (clockwise) direction again, and press “Take Reading” after the position reading has stabilized.
10. Repeat steps 8 and 9 one more time. There should now be six numbers displayed in the calibration screen boxes. When the last reading is taken, a calibration constant will be calculated and displayed in the lower right portion of the window. Note this number and click “Ok” to return to the DilaSoft main screen.
11. Click on the Instrument tab, then press the Set Channels button. A Channel Setup screen will appear. The calibration constant noted in step 10 should match the calibration constant displayed under the Scale column for Channel 0.
12. Remove the retaining clip and turn the micrometer until it is fully retracted from the ball end of the LVDT, leaving a gap of at least 3mm between the micrometer and ball.

3.1.2.2.2 Complete Calibration

Proceed with the same steps as in the Check Calibration procedure above with the following exception: When the last reading is taken and the calibration constant is calculated, pressing the “OK” button will save the calibration constant in the calibration file. Verify that the calibration constant has been saved by doing the following:

1. Note the calibration constant after the calibration procedure has been completed. Then press “OK” to exit the calibration screen and return to the main DilaSoft screen.

2. Click on the Instrument tab, then press the Set Channels button. A Channel Setup screen will appear. The calibration constant noted in step 1 should have been automatically entered into the first line (Channel 0) under the Scale column. If the number in this position does not match the calibration constant obtained by the calibration procedure, enter this number and press “OK”.

3.1.2.3 Liquid Helium Dewar

The Cryofab 100 L liquid helium dewar has three main valves, V1, V2 and V3, as shown in Figure 3.4.

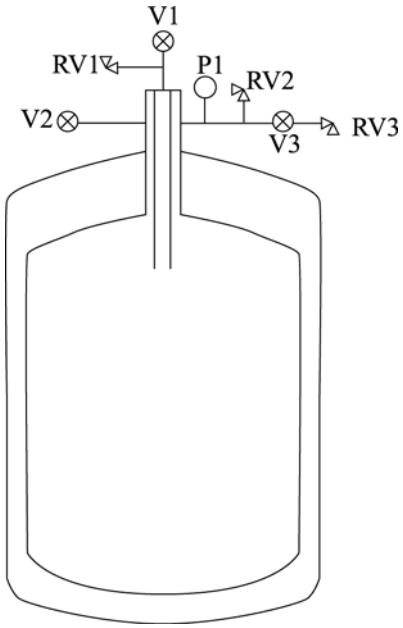

Figure 3.4: Helium dewar schematic.

The V1 valve shown in the figure is the liquid valve for withdrawal tube access to the liquid helium reservoir. V2 is the vent valve, and V3 is the isolation valve. RV1 is a 15 psig relief

valve, RV2 is a 10 psig relief valve, and RV3 is a 0.5 psig relief valve that only operates when the isolation valve (V3) is in the OPEN position. P1 in Figure 3.4 is the pressure gauge. The net evaporation rate for this dewar is 1% volume per day. Specifications for dilatometer operation indicate a consumption rate of 1.5 L to cool down the withdrawal tube, and 0.55 L/hr at 4.2 K. Before proceeding with liquid helium operation, check the following:

1. Make sure the 12 mm quick coupling is properly installed into the entry port (V1) at the top of the dewar.
2. Verify that the isolation valve (V3) is open.
3. Make sure the vent valve (V2) is closed.
4. Check the dewar pressure gauge (P1) and make sure the pressure does not exceed 1 psig. If the pressure gauge exceeds 1 psig and the isolation valve is open, this may be indicative of a blocked relief valve and could present a hazardous situation. Contact Cryofab for assistance.

3.1.2.3.1 Liquid Helium Level Check

Note: If the transfer tube is already inserted into the dewar and you are certain the level of liquid helium is adequate for this test, the steps in this section may be skipped.

CAUTION: GAS ESCAPING FROM THE DEWAR THROUGH THE V1 VALVE IS EXTREMELY COLD. DO NOT ATTEMPT THIS PROCEDURE WITHOUT WEARING ADEQUATE PROTECTIVE CLOTHING ON THE FACE, HANDS AND BODY.

1. Open the V1 valve on top of the dewar and very slowly insert the flutter tube until it reaches the bottom of the dewar.
2. Attach a clip to the flutter tube just above the dewar entry port while the tube is touching the bottom.
3. Note the oscillation of the rubber membrane while tube is touching the bottom of the dewar. Slowly pull the tube upward out of the dewar while monitoring the membrane oscillation.
4. At the point when the membrane oscillation increases noticeably, attach another clip to the flutter tube just above the dewar entry port.
5. Withdraw the flutter tube completely from the dewar, and close the V1 valve on top of the dewar. Measure the distance between the two clips on the flutter tube. This distance is the level of liquid helium in the tank (Refer to the calibration chart on the top of the dewar for conversion). Make sure this distance is at least 14 cm* before proceeding.

*This value may need to be modified after verifying consumption rates for typical experiment runs.

3.1.2.4 Cool Down Transfer Tube

Note: This procedure requires 3 people.

Note: This procedure requires a ladder in order to insert the withdrawal leg of the transfer tube vertically down into the dewar.

CAUTION: UNDER NO CIRCUMSTANCES SHOULD THE TRANSFER TUBE BE HELD UP BY THE WITHDRAWAL LEG. THIS CAN CAUSE THE LEG TO BECOME BENT, AND WILL RESTRICT OR PREVENT FLOW OF LIQUID HELIUM.

1. Close the needle valve on the transfer tube by rotating it clockwise. Then open it by turning it counter-clockwise a maximum of 4 turns.
2. Unscrew the brass tip from the delivery end of the transfer tube and connect a high purity helium gas source to the end of the tube. Purge the transfer tube with helium gas for a few minutes, and then disconnect the gas source from the tube. Reinstall the brass tip.
3. Fully open the valve on the VC31 gas flow controller by turning it counter-clockwise.
4. Supporting the transfer tube from the elbow, insert the withdrawal leg until it just contacts the ball of the V1 valve. Have a second person open the valve, and very slowly insert the transfer tube into the dewar. As the tube is being lowered, have a third person insert the other end of the transfer tube into the cryostat arm. As the transfer tube leg is lowered into the dewar, it will cause some helium to boil off and raise the pressure inside the dewar. The 0.5 psig relief valve will periodically vent as the transfer tube leg is being lowered into the dewar. **Carefully monitor the dewar pressure to ensure it does not rise above 7.25 psig.** Use the vent valve to lower the pressure if necessary.

   CAUTION: DO NOT OPEN ANY VALVES ON THE DEWAR IF THE PRESSURE GAUGE ON THE DEWAR READS BELOW ZERO. AN INFLUX OF AIR WILL CAUSE ICE TO FORM INSIDE THE DEWAR WHICH CAN BLOCK VENT VALVES, LEADING TO A DANGEROUS OVERPRESSURIZATION CONDITION.

5. When the transfer tube has been fully inserted, tighten the coupling nut at the top of the dewar to create a seal around the tube. Do not tighten the knurled nut on the cryostat end of the tube. This allows the helium flow to bypass the cryostat and cool down the transfer line more quickly.
6. Switch on the GF3 pump, and connect the suction line to the exhaust port on the transfer tube. Monitor the helium flow on the gas flow controller gauge. The flow rate should increase gradually as the tube cools.
7. After several minutes when the flow rate reaches 1.5 L/hr, tighten the knurled nut on the cryostat end of the transfer tube. Check this connection periodically, as differential thermal contraction of components may cause the nut to loosen.
8. The flow rate on the VC31 meter will drop when the cryostat nut is tightened due to the resistance of the flow through the cryostat heat exchanger. As the cryostat cools, the flow rate should eventually reach 1.5 L/hr again.
9. If the flow rate does not reach 1.5 L/hr after 20 minutes, the tube may be blocked. Refer to the Troubleshooting section.

3.1.2.5 Running the Experiment

3.1.2.5.1 Writing the Temperature Program

1. Open the DilaSoft software and click on the Program tab. The most recent temperature program will be shown in the box. Click on the “Change” button.

2. If this will be a new program, click on the "New" button at the top of the window. The software will then ask you to name your temperature program. Type in the sample material followed by a dash, followed by the reference material, followed by a six-digit date (e.g., November 9, 2005 would be 110905). Click the Save button.
3. Double-click on the first blank segment in the window. This will open an editing window.
4. The first step in the temperature program should be as follows:
    a. Ramp: 0 °C/min
    b. To: (enter the temperature shown on the Eurotherm on the top)
    c. Hold: 2 minutes
    d. Storage interval: 10 s.

    This step will allow the temperature to stabilize before beginning the cooling segment. Click "OK".
5. Double-click on the first line of the program you just entered. The edit window will open again. Enter the parameters for the next program segment. The "Ramp" value should not be more than 3 °C/min. Enter a "Hold" time of several minutes to allow the sample temperature to "catch up" to the program temperature if there is a difference between the two. When you are finished entering parameters for this step, click "Insert After" or "Insert Before" as appropriate to add this step to your temperature program.
6. Continue adding more steps in the same manner. The window below will display a graphical representation of the temperature program steps. *Note: The lower temperature boundary for the copper reference is -253 °C; the lower boundary for fused silica is -193 °C. During execution of the program if the sample temperature exceeds the upper or*

lower limits of the reference being used, the program will automatically terminate as a safety feature. If the temperature program must exceed these limits, define the reference material on the Main menu as "unknown".

7. Make sure that the last step in your temperature program has the "Use Exit Temp" box checked. This will return the furnace to the preset exit temperature (25 °C, in this case) when the experiment has ended.
8. The "Delete" button in the edit window can be used to remove a step in the temperature program.
9. When all the steps of the temperature program have been entered, click the "Save" button, then click "Exit" to return to the main DilaSoft menu.

3.1.2.5.2 Setting the Experiment Parameters

1. From the DilaSoft Main Menu, select the "Main" tab. This will display the current Test Data, Experiment Data and Reference Data.
2. Click on the "Change" button. This will bring up the Dilatometer Experiment Setup screen. Enter your name in the box next to "Operator".
3. Click on the arrow to the right of the "Temp Prog" box and choose "Select" from the drop down menu. This will bring you to a list of program files. Select the name of the temperature program file you created and click "Open".
4. Click on the arrow to the right of the Data File box. This brings up a window where you can enter a data file name. Follow the same file naming format as the temperature program (specimen material, dash, reference material, date), and click on Save. If the

same experiment is run more than once on the same date, add a dash and a sequential number to the data file name so that the previous data file will not be overwritten when the experiment is run again.

5. Click on the "Save Exp File As" button at the bottom of the Dilatometer Experiment Setup screen. Follow the same file-naming format as described in the previous step to give the experiment file a name. Click on Save.
6. The Comments button brings up a window into which comments regarding the experiment can be entered. The comments will appear in the printed experiment reports.
7. In the Specimen Data section, type the name of the specimen material. From the drop down menu under the specimen name, select the type of material from the list. If the material is not listed, select "unknown".
8. Enter the exact length of the specimen in the Length box in the Specimen Data section.
9. In the Reference Data section, select the appropriate reference material from the drop down menu. If the lower temperature limits of the reference material will be exceeded during this experiment, select "unknown" for the reference data, even if the material is known. This will prevent program termination if the sample temperature becomes lower than the limits of the reference material data.
10. Enter the exact length of the reference material in the Length box in the Reference Data section. This value is listed on the box lids of the NIST reference materials included with the dilatometer.
11. Make sure the furnace is switched OFF during the cooling portion of the temperature program.

3.1.2.5.3 Running the experiment

1. Click the "Start" button to start the experiment. The DilaSoft Run-Time display will appear, and a Check Instrument box will appear. Click OK. *Note: the Check Instrument box tells you to make sure the furnace is turned on. Disregard this and leave the furnace turned off for the cooling portion of the temperature program.*
2. The LVDT Position window will appear which displays the current position reading and specimen temperature. The temperature program will not begin until the "OK" button is clicked in this window.
3. As the experiment is running, the window will display various parameters. The graph displays temperature along the left axis, expansion along the right axis, and time along the bottom axis. The temperature shown is the specimen temperature, which should be approximately the same as the topmost temperature displayed on the Eurotherm unit on the power controller. (If these numbers do not match, consult the Temperature Correction Table in section 6 of the green Theta manual to obtain the conversion). The Set Point temperature is the temperature that is dictated by the program. It will precisely follow the Ramp (°C/min) that was entered in the current temperature program step. The temperature indicators on the right side of the window show the set point temperature (program temperature) on the left and the specimen temperature on the right. The levels will be shown in red for heating program segments, and blue for cooling program segments. The bottom of the window shows the temperature program segment currently being run. These segments can be edited while the program is running simply by double-

clicking on the segment, double-clicking on the segment again in the Temperature Program box, changing it, and clicking “OK”.

3.1.2.6 Warming up the System

1. Switch the furnace ON when the temperature program reaches the heating portion.
2. Switch OFF the GF3 pump.

3.1.2.7 Shutting Down

After completion of an experiment, the following steps should be taken to ensure proper shutdown of the system.

1. Make sure the GF3 pump is switched off.
2. Switch off the furnace and the power control switch.
3. Disconnect the stiff plastic tube (connected to the transfer tube outlet port) from the back of the VC31 gas flow controller. This will allow any helium left in the system to expand freely and vent from the system.
4. Completely close the needle valve on the transfer tube.
5. On the helium gas cylinder, turn the regulator valve (the smaller of the two knobs) clockwise until it is completely closed. Close the valve on top of the helium gas cylinder by turning it clockwise until it is completely closed.
6. DO NOT open the sample space until it has warmed up to room temperature. Opening the sample space while it is still below freezing will allow condensation to freeze on the inner surfaces of the sample space.

7. If more experiments will be run in the near future, leave the transfer tube inserted into the dewar, and make certain that the V3 isolation valve on the dewar is open.
8. If no further experiments are to be run in the next several days, remove the transfer tube from the system by completing the following steps: *(Note: This requires 3 people.)*
    a. Completely loosen the knurled nut which attaches the cryostat arm to the transfer tube.
    b. Loosen the coupling at the top of the helium dewar so that the dewar leg can be withdrawn.
    c. While one person begins to lift the delivery end of the transfer tube from the cryostat, a second person lifts the withdrawal leg from the dewar.

       CAUTION: THE TRANSFER TUBE WITHDRAWAL LEG WILL BE EXTREMELY COLD WHEN IT IS WITHDRAWN FROM THE DEWAR, AND CAN CAUSE DAMAGE TO THE SKIN. TAKE ALL PRECAUTIONS NECESSARY TO ENSURE THAT IT DOES NOT COME INTO CONTACT WITH ANY BARE SKIN UNTIL IT HAS WARMED SUFFICIENTLY.
    d. As soon as the withdrawal leg is pulled out above the ball valve, have a third person close the valve to help minimize pressure loss in the helium dewar.
    e. When the transfer tube has been withdrawn from both the dewar and the cryostat, move it to an appropriate storage location (inside its original shipping box or supported by appropriate retaining hangars).
    f. Insert the dust plug into the top of the cryostat arm, and insert the brass plug into the top of the dewar coupling.

9. Turn off the water circulation pump if it was used during the experiment.

3.1.2.8 Troubleshooting

Flow does not increase to 1.5 L/hr after 20 minutes. This may be indicative of a blockage in the transfer tube. Tighten/loosen the knurled nut at the cryostat end, and note whether this produces a change in the flow rate indicated on the VC31 float gauge. If it does not, the tube may be blocked. Remove the transfer tube from both the dewar and the cryostat, being very careful to avoid any contact with the transfer tube's dewar leg (it will be EXTREMELY cold and can damage the skin). Allow the transfer tube to warm up to room temperature (several hours or overnight). Attach a balloon or equivalent to the dewar leg, covering the inlet holes. Remove the small brass tip at the delivery end of the transfer tube by carefully unscrewing it. Attach a high purity helium gas source to the delivery end of the tube. Allow the high purity helium gas to flow through the tube and verify that the balloon at the other end inflates. *Note: if a balloon or equivalent is not available, submerge the dewar leg of the transfer tube in a small beaker of alcohol, and watch for the appearance of bubbles as the helium gas is flowed through the tube.* Alternatively, a length of 30# fishing line (0.55 mm diameter) may be used to check the tube for blockage. Remove the brass tip from the delivery end of the transfer tube, and carefully thread the fishing line up into the tube. When no more line can be fed into the tube, mark the end of the fishing line and withdraw it from the tube. Use the mark to determine how far through the tube it was able to pass. If both of these techniques indicate no blockage problems, contact Oxford Instruments for further assistance.

Program temperature is substantially different from the actual sample temperature. During the cooling phase of the temperature program, the cooling rate is controlled entirely by the flow rate of the liquid helium into the cryostat, and not by the furnace. Therefore, the cooling rate may be different from the one entered into the temperature program. The temperature program can be adjusted while it is being run

3.1.2.9 Recommendations

3.1.2.9.1 Water Circulator Modifications

Extended period use of the water circulation pump (more than one hour) has been found to result in a gradual increase of the water temperature due to the submerged pump heating the water. If the water circulation system is to be used on a regular basis (i.e., if the ambient air temperature fluctuates by more than 2 °C during the course of a test run), one of the following is recommended: 1) Remove the water pump from the water reservoir, connect a tube with one end attached to the pump inlet and the other end submerged in the water reservoir, and leave the outlet hose (the one bringing water *from* the instrument head into the reservoir) connected as-is; or 2) Leave the current configuration as-is, but add ice to the reservoir to compensate for the pump operation heating the water.

3.1.2.9.2 Low-flow Regulator

More precise control of the helium gas flow through the sample chamber may be better achieved by installing a regulator capable of very low flow rates. The low-flow regulator may either entirely replace the two-stage regulator currently on the helium gas cylinder, or may be of the type which can be installed in-line with the two-stage regulator, downstream of the flow.

3.1.2.9.3 T-junction for helium gas

A T-junction and isolation valve may be installed on the ¼" helium gas tubing in order to make purging of the transfer tube more conveniently achievable without having to disconnect the helium gas line from the instrument head inlet port.

3.1.2.9.4 Liquid Nitrogen Operation

There are several advantages to operating the dilatometer with liquid nitrogen instead of liquid helium, the most significant of which is cost savings. However, a few modifications to both equipment and procedures must be made to accommodate the more viscous liquid nitrogen.

3.1.2.9.4.1 Equipment Modifications

A dedicated liquid nitrogen dewar with a top-loading withdrawal valve is necessary for this configuration. Since liquid nitrogen is more viscous than liquid helium, the nitrogen dewar must maintain a positive pressure to allow the nitrogen to be drawn up through the small

capillary in the LLT transfer line. A self-pressurizing dewar would be the most convenient option for maintaining sufficient pressure during operation.

Additionally, the VC31 gas flow controller must be replaced by a VC41 controller. The VC31 is calibrated for helium gas only, and will not give the correct flow readings for nitrogen. The VC41 is calibrated for both helium and nitrogen gases.

3.1.2.9.4.2 Procedure Modifications

The liquid nitrogen must be drawn through the system at a slower rate than the helium, so the cooldown procedure will require more time. During operation, the nitrogen dewar should be pressurized to approximately 5 –10 psi. When the GF3 pump is switched on, begin with the flow controller valve closed and open it slowly while monitoring the pressure gauge. Ensure that the pressure does not drop lower than 150 mbar, or the nitrogen may freeze and cause a blockage in the cryostat. During the cooling procedure, the float in the nitrogen flow meter should rise up to 600-700 mbar after about 20 minutes. It may be necessary to continuously pump the outer vacuum chamber of the cryostat during the experiment, since the liquid nitrogen is not cold enough to effect cryopumping.

3.2 Differential Scanning Calorimeter Testing

In addition to dilatometry, differential scanning calorimeter (DSC) testing was also employed as a characterization method for Ni-Ti-Fe. The DSC (see Figure 3.5) measures heat flow vs. temperature for a sample, and is therefore able to detect phase changes, which register as endothermic or exothermic peaks. The DSC used for the characterization experiments of Ni-

Ti-Fe is a Perkin-Elmer Diamond DSC, capable of temperatures as low as –160 °C and as high as 730 °C.

The sample is crimped into a small aluminum sample pan, and placed into the sample holder on the left side, and an empty crimped aluminum pan of the same size is placed into the reference holder on the right. The DSC measures precisely how much heat is required to raise the temperature of both the sample and the reference at the same heating rate. When the sample undergoes a phase change (melting, for example), extra heat is required to be added to the sample in order to accommodate the latent heat requirements for melting. The extra heat that must be added to the sample holder side is not added to the reference side, which is not undergoing a phase change and continues a steady increase in temperature. The difference in heat flow between the sample and the reference registers on the temperature vs. heat flow plot as an endothermic peak, since the sample required more heat to keep it at the same temperature as the reference.

Similarly, a sample undergoing a freezing phase change gives off extra heat during this process. It therefore registers as an exothermic peak on the plot. Solid-state phase changes, such as the austenite → R-phase and the reverse transition, also appear as exothermic and endothermic peaks, respectively. The temperatures at which the endothermic and exothermic reactions occur on the plot make it possible to accurately determine the phase transition temperatures as well as the temperature hysteresis for shape-memory alloys.

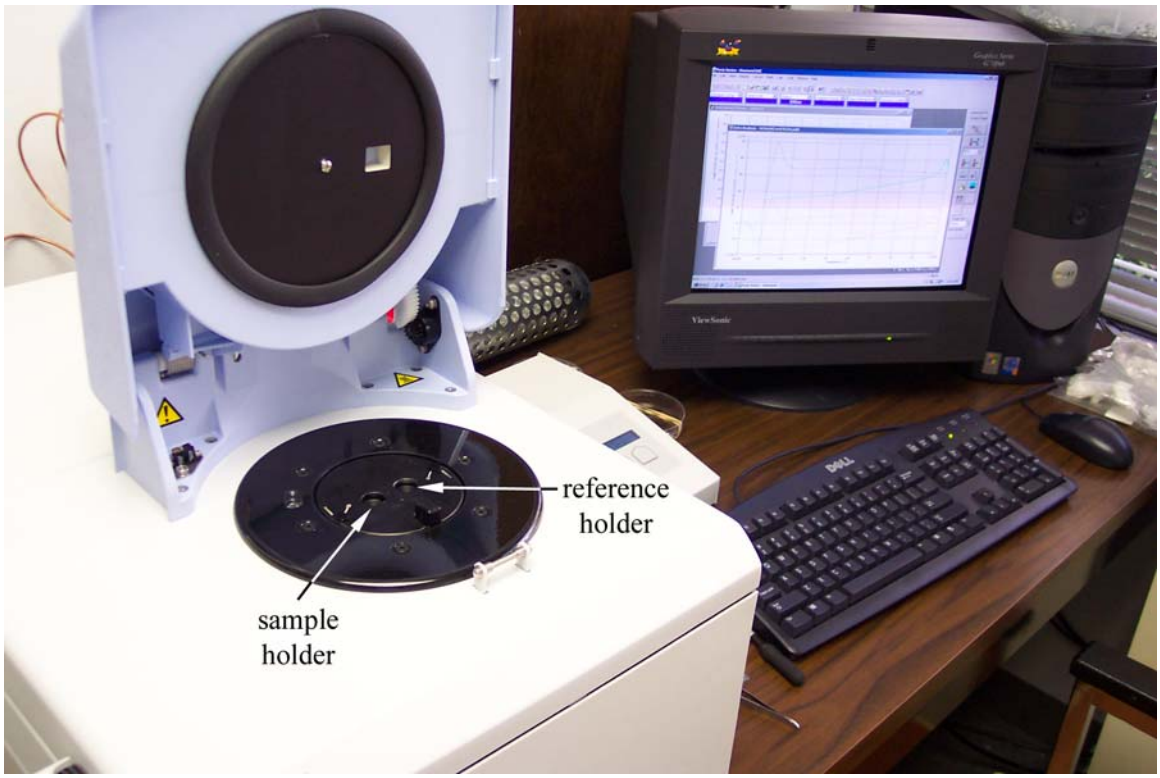

Figure 3.5: Differential Scanning Calorimeter (DSC).

Although the martensitic transition temperature of the Ni-Ti-Fe alloy was lower than the temperature capabilities of the DSC, the R-phase transition temperature occurred well within the measurement range of the instrument. DSC measurements were therefore carried out on several samples of Ni-Ti-Fe that were subjected to different heat treatments in order to understand how the heat treatments affected the R-phase transition. Most shape-memory alloys employed as actuators are required to be shape set in a particular shape for use as an actuator element. Since NiTi alloys are commonly used, there are several well-documented procedures for shape-setting it at a particular temperature for a particular period of time. No such documented procedures for Ni-Ti-Fe are publicly available, however, so some limited experimentation to this effect was

accomplished, the results of which are documented in Chapter 5. For the current conduction switch configuration, the additional shape-setting heat treatment was unnecessary; the solutionizing treatment alone was adequate for the switch to function properly. Shape-setting heat treatment experimentation was not the focus of this work, but was carried out as a preliminary investigation in order to gauge the effects on the transformation temperatures and shape memory characteristics of Ni-Ti-Fe.

CHAPTER FOUR: NI-TI-FE SWITCH TESTING

The Ni-Ti-Fe thermal conduction switch is the fourth in a series of SMA thermal conduction switch designs. Figure 4.1 shows the progression of switch designs:

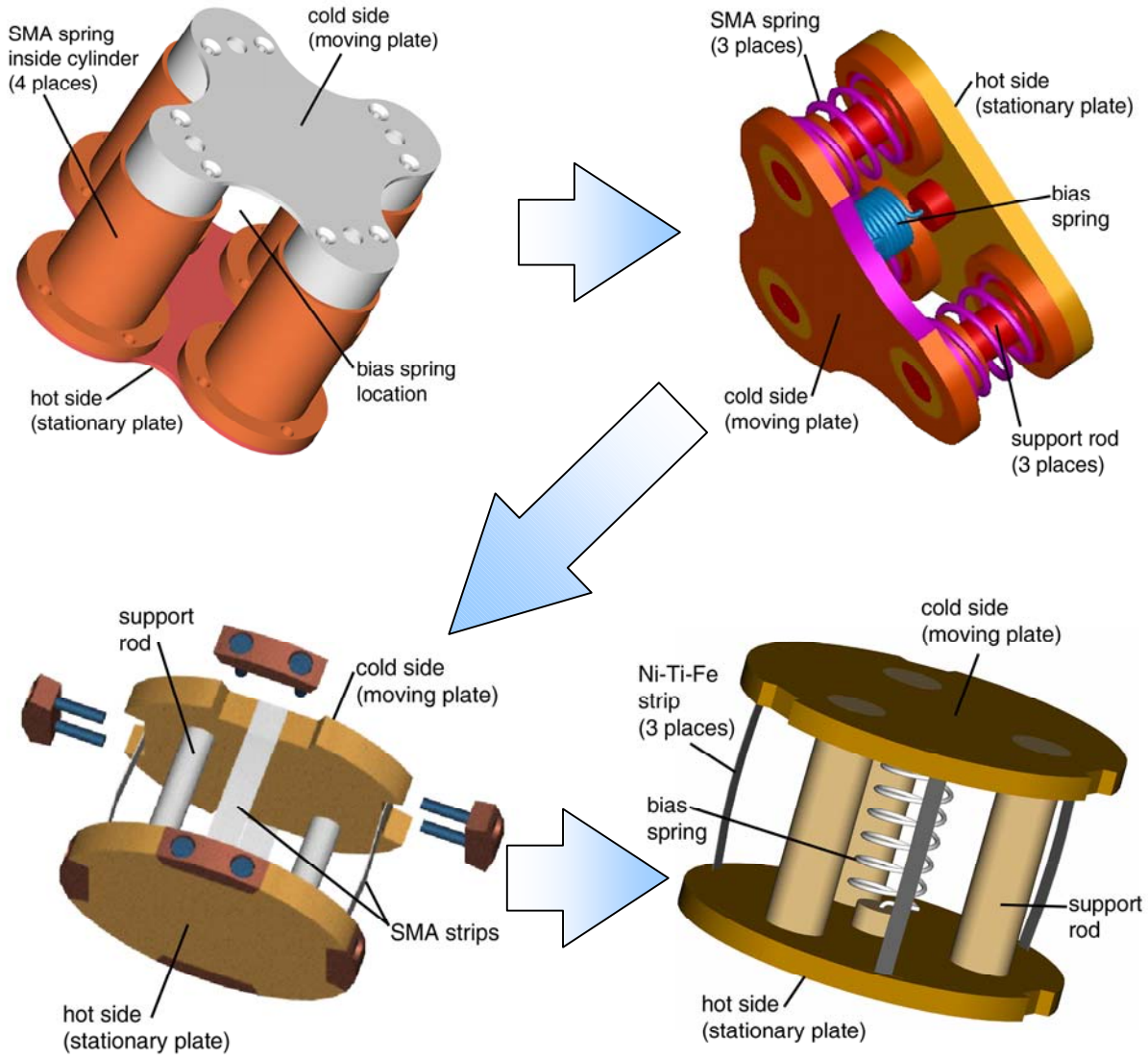

Figure 4.1: SMA thermal conduction switch design progression [Droney *et al.* 2003; Krishnan 2003].

The first version, developed by the author and co-workers [Droney *et al*. 2003], was a proof-of-concept prototype that used a commercially available NiTi alloy to fabricate the actuation springs, located inside each of the four cylinders. It was designed to operate at ambient and above ambient temperatures. The next version used thermomechanically treated NiTi wire whose transformation temperature was much lower than the first version. This switch operated at cryogenic temperatures. The third version also operated at cryogenic temperatures, and used commercially available NiTi SMA strips instead of wire springs as the actuation elements, which offered the advantage of ease of fabrication. The current version also uses SMA strips as the actuating elements. Unlike the third version, however, the SMA strips are made of a custom Ni-Ti-Fe alloy, whose R-phase transformation characteristic serves to minimize the temperature hysteresis that has been a factor in all three previous designs.

The particular Ni-Ti-Fe alloy chosen for the thermal conduction switch is $Ni_{46.8}Ti_{50}Fe_{3.2}$. It was purchased from Special Metals in the form of a large, vacuum-induction-melted and vacuum-arc-remelted billet. The samples used for testing and the strips used in the switch were cut from the billet by means of electrical discharge machining (EDM), which has the advantages of high precision and insignificant heating of the material during the cutting process.

4.1 Concept and Operation

The basic principle behind the operation of the Ni-Ti-Fe thermal conduction switch is a repeated cycling of the SMA elements between the R-phase and the austenite phase, which ultimately causes the switch to expand and contract. The “open” and “closed” positions of the switch are shown in Figure 4.2.

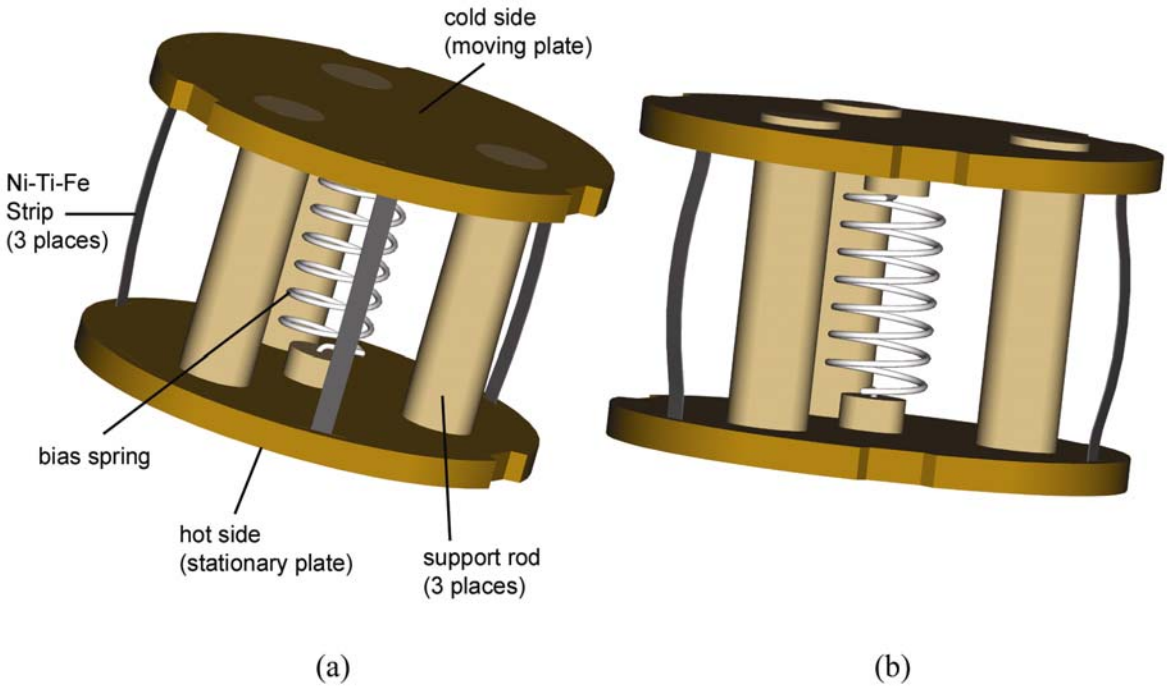

Figure 4.2: Ni-Ti-Fe switch in the closed (extended) position (a) and the open (contracted) position (b).

The switch is designed to operate between dewars of liquid methane at 118 K and liquid oxygen at 92 K. It is assumed in this scenario that the liquid oxygen dewar's temperature is maintained by a cryocooler or another such temperature control device. Therefore the liquid oxygen dewar is regarded as a heat sink for the liquid methane dewar. The stationary plate of the switch is mounted securely against the liquid methane dewar such that good thermal contact can be maintained. A layer of indium foil between the dewar and the stationary plate can also be employed to help decrease thermal contact resistance. When the switch is at a temperature below the R-phase transformation temperature of the Ni-Ti-Fe strips, the strips can be bent more easily due to twinning in the material [Shmalo 2005]. The force of the bias spring, in this state, causes

the strips to bend more in their buckled shape, which in turn contracts the movable plate toward the methane dewar. This configuration is shown in Figure 4.2(b).

As the liquid methane dewar temperature increases over time, the heat is conducted into the Ni-Ti-Fe switch. Eventually the SMA elements are heated to a temperature sufficiently high enough to cause the material to undergo a phase transformation from the R-phase to the austenite phase. When this happens, the Ni-Ti-Fe strips become more rigid, and impart additional force against the bias spring. This causes the movable plate to expand outward until it makes thermal contact with the liquid oxygen dewar, as shown in Figure 4.2(a). A layer of indium foil between the movable plate and the liquid oxygen dewar helps ensure good thermal contact between the switch and the dewar.

While the switch is in the extended position, thermal contact between both dewars provides a conduction path across which heat is dissipated from the warmer liquid methane dewar into the colder liquid oxygen dewar. Eventually as the liquid methane dewar cools, the temperature of the conduction switch will decrease until it falls below the R-phase transformation temperature of the Ni-Ti-Fe strips. The strips then undergo a phase change from austenite to R-phase, causing them to become weaker and more susceptible to the bias spring force. When this happens, the strips buckle to a greater degree, causing the movable plate to break thermal contact with the liquid oxygen dewar, and contract towards the liquid methane dewar as in Figure 4.2(b). The cycle repeats itself, thus maintaining the temperature of the liquid methane.

4.2 Configuration

In order to ensure proper switch actuation, consideration must be given to the force balance between the bias spring and the SMA elements. The spring must not be so stiff that it prevents movement of the SMA strips as they undergo phase changes, and it must be stiff enough to be able to overcome the stiffness of the SMA elements when they are in the "softer" R-phase. The force generated by the bias spring in maximum extension was calculated to be 20.7 N, as shown below:

x_e = 18.71 mm (length of extended spring)

x_c = 9.88 mm (length of contracted spring)

$\Delta x = x_e - x_c$ = 8.83 mm

G = 69 GPa (modulus of rigidity)

n = 6 (number of active coils)

d = 1.63 mm (diameter of wire)

D = 16.29 mm (diameter of spring)

Spring constant:

$$k = \frac{G \cdot d^4}{8 \cdot n \cdot D^3} = 2.34744 \frac{N}{mm} \quad (1)$$

Force imparted by bias spring when extended 8.83 mm:

$$F = k \cdot \Delta x = (2.34744 \text{ N/mm}) \cdot (8.83 \text{ mm}) = 20.7279 \text{ N} \quad (2)$$

$$F/3 = 6.90936 \text{ N} \quad \text{(force imparted on one Ni-Ti-Fe strip)} \quad (3)$$

Since there are three strips in this configuration, there is a force of 6.9 N per strip, as shown in Equation 3.

The force required to buckle a single SMA strip was calculated using the Euler equation for buckling of slender columns, as shown below:

l_y = 76.44 mm (length of strip)

l_x = 0.41 mm (thickness of strip)

l_z = 3.25 mm (width of strip)

E = 72 GPa (modulus of elasticity)

$A = l_x \cdot l_y$ = 1.333 mm^2 (cross sectional area)

Moment of inertia:

$$I_y = \frac{l_y \cdot l_x^{\,3}}{12} = 0.439027 \text{mm}^2 \tag{4}$$

$$I_x = \frac{l_x \cdot l_y^{\,3}}{12} = 1.526 \cdot 10^4 \text{mm}^2 \tag{5}$$

Radius of gyration:

$$r = \sqrt{\frac{I_y}{l_x \cdot l_y}} = 0.118357 mm \tag{6}$$

Effective slenderness ratio (assuming both ends fixed):

$$k = 0.65 \tag{7}$$

$$S = \frac{k \cdot l_y}{r} = 419.798 \tag{8}$$

Buckling for slender columns (Euler's equation):

$$F = \frac{A \cdot \pi^2 \cdot E}{S^2} = 5.373\text{N} \tag{9}$$

The force required to buckle a single strip is 5.373 N, as indicated in Equation 9. Therefore the force imparted by the bias spring is adequate to cause buckling.

If the force on the SMA strips is too great, it can cause them to fail. During one experiment run to measure switch displacement, approximately 19.4 N of additional force was placed on the SMA strips, in addition to the 20.7 N from the bias spring. The additional force was added while the SMA strips were in the R-phase, which caused an increase in total switch displacement. However, as the temperature of the strips increased and they transformed into the more brittle austenite phase, the strips failed at the location of maximum stress.

A simulation was run using I-DEAS Master Series 9 to model the stress profile of a single Ni-Ti-Fe strip with one-third the force of the bias spring applied. The results are shown in Figure 4.3.

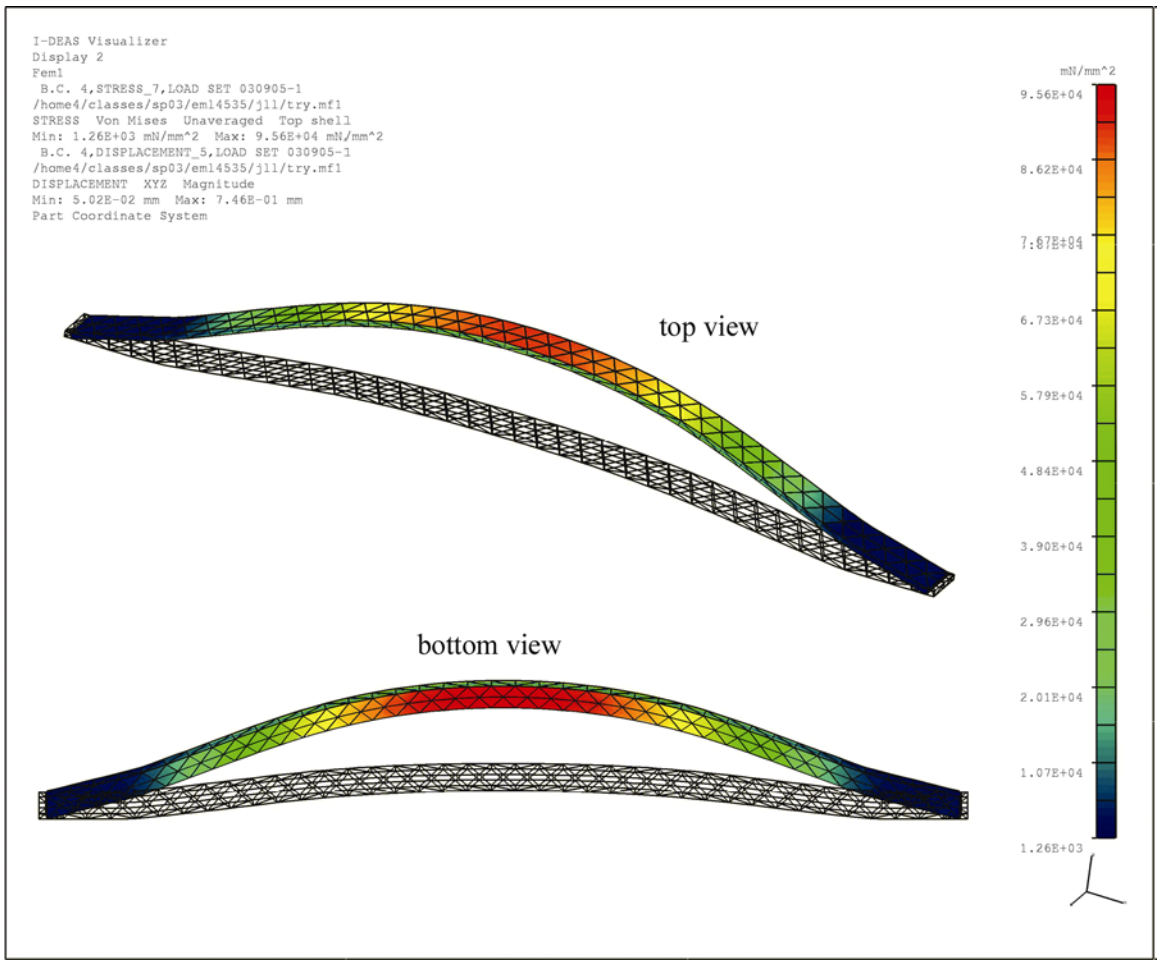

Figure 4.3: Stress profile of a Ni-Ti-Fe strip.

The results of the simulation show a maximum stress of 95.6 MPa at the midpoint of the strip in its buckled configuration under the load of the bias spring. The maximum stress location is consistent with the location of the failure point during the experiment run when additional force was added to the strips.

In addition to predicting the point of failure of the strips, awareness of the stress gradient is also important in understanding its influence during phase transformations. Since both stress and temperature gradients can induce a phase change, they both play a role in determining which

areas of the strips will transform into the R-phase first during switch cycling. Figure 4.4 illustrates the areas that transform first and last during the austenite → R-phase transformation (a) and the reverse transformation (b).

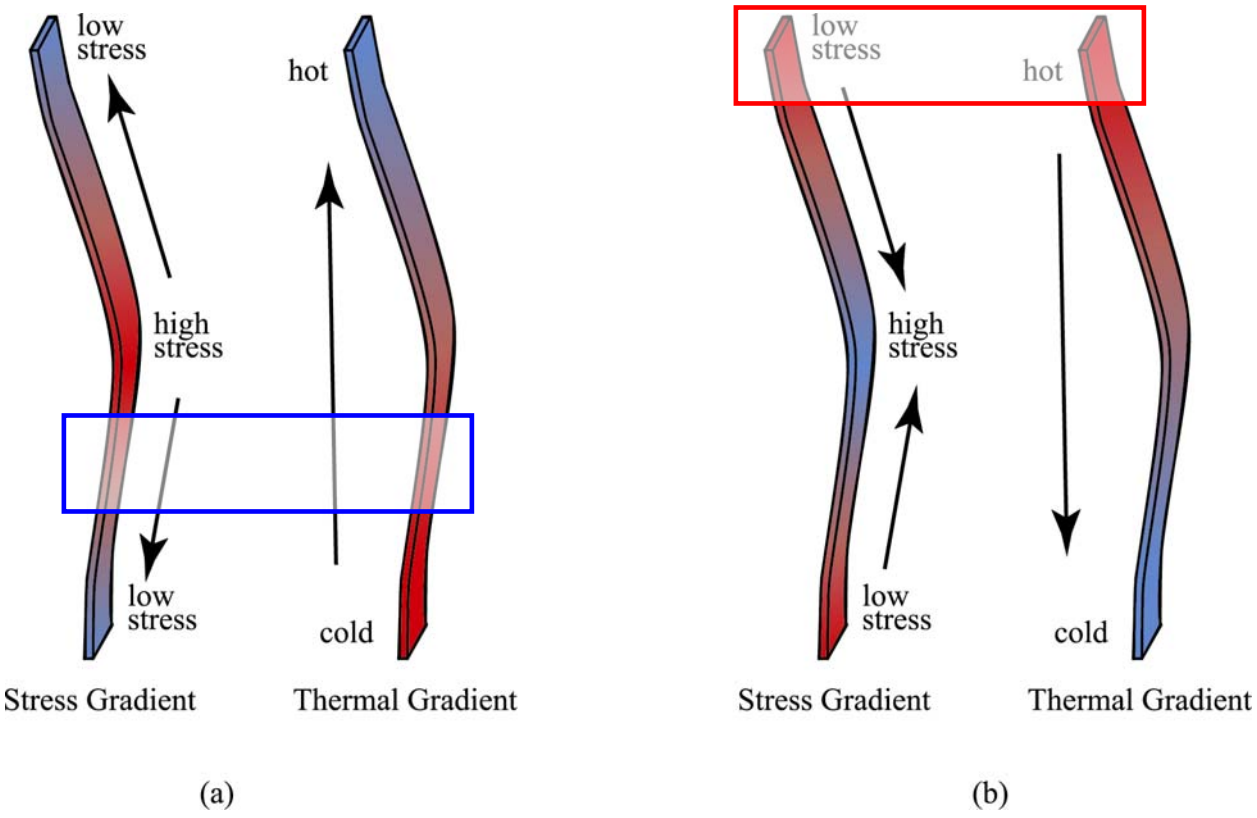

Figure 4.4: Influence of thermal and stress gradients on transformation.

The transformation proceeds in the direction of the arrows. The overall effect from both gradients indicates that during the austenite → R-phase transformation (a), the area in the blue box just below the mid-point where the greatest concentration of stress and cold exists will transform to the R-phase first. During the reverse transformation (b), the areas of lowest stress and highest heat (in the red box) will transform to the austenite phase first.

To help achieve maximum displacement of the switch during actuation, the strips were installed in a pre-buckled configuration. When the strips transformed into the R-phase in their pre-buckled configuration, all the force from the bias spring was devoted to increasing the magnitude of the buckle, as opposed to most of the force being devoted to buckling the strips initially. Pre-buckling the strips also provided the advantage of being able to control the direction of the buckle (inward or outward), which helped ensure symmetrical movement of the switch.

4.3 Outside Chamber Testing

In order to gain an initial understanding of the performance of the switch, testing was conducted outside the simulation chamber using liquid nitrogen to cause actuation of the SMA strips. The goal of these experiments was to verify the switch performance in terms of temperature hysteresis, and to obtain an initial estimate of the magnitude of the displacement of the switch. In order to determine hysteresis, data points for both the heating and cooling portions of the thermal cycle were needed. Since the temperature and displacement changes happened very rapidly during the cooling portion of the cycle, the experiment was digitally recorded and the data points were collected from the recording. Further testing was conducted inside a controlled testing chamber, which simulates more closely the temperature gradient over which the switch is designed to perform. This testing is discussed in section 4.4.

4.3.1 Outside Chamber Test Configuration

The test configuration is shown in Figure 4.5.

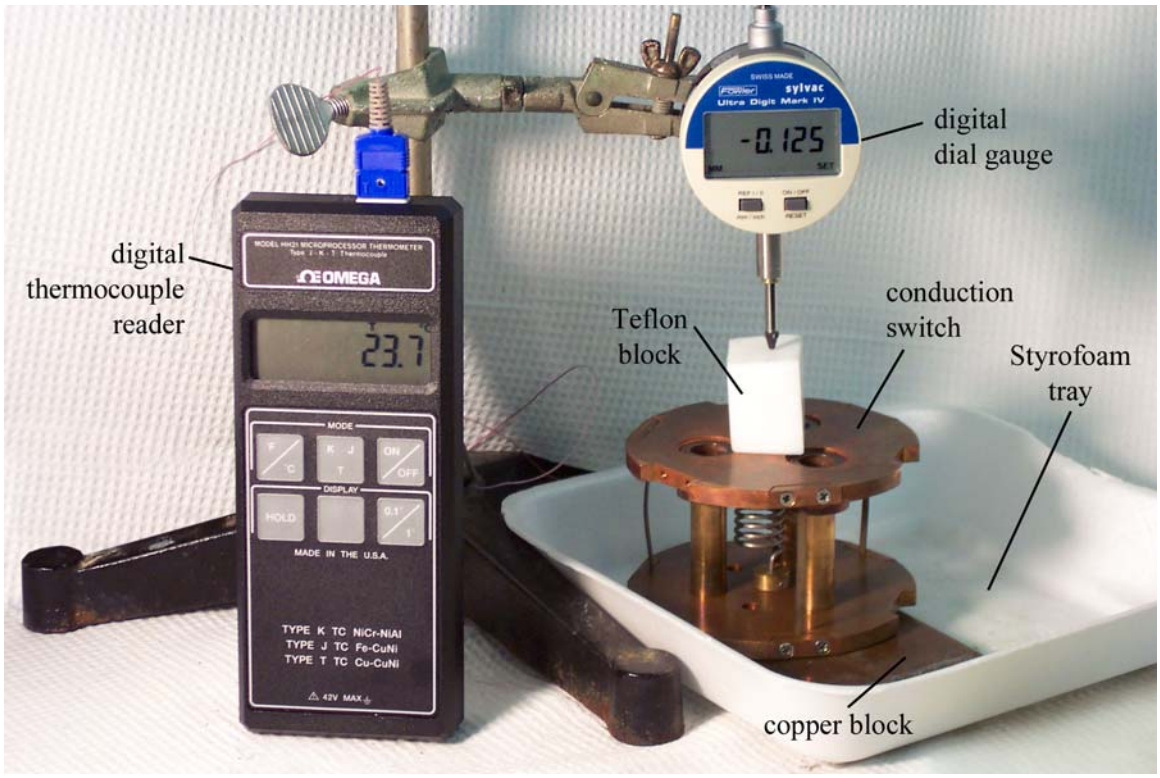

Figure 4.5: Outside chamber test setup.

The switch was placed in a Styrofoam tray, and liquid nitrogen was poured into the tray. Initial experiment runs showed false displacement readings associated with the boiling of the liquid nitrogen pushing upward on the bottom surface of the switch. For later experiments, placement of the switch on top of a copper block with holes cut into it proved to minimize the "floating" effect of the boiling nitrogen on the switch. A block of Teflon was placed between the digital dial gauge and the top of the switch to insulate the instrument from the extremely cold temperatures, which could have affected the accuracy of the readings. Liquid nitrogen was poured into the Styrofoam tray until the liquid level just reached the top surface of the bottom plate of the switch. The nitrogen was then allowed to boil off and the switch to warm up to room

temperature. The digital dial gauge was initialized at 0.000 mm at room temperature before the test began. As the switch compressed, the gauge read a negative displacement. Temperature and displacement data were obtained for the entire thermal cycle.

4.4 Inside Chamber Testing

In order to more closely approximate the actual environmental conditions of the thermal switch, a custom cryogenic chamber was built by V. Krishnan in 2003. The chamber has provisions for a liquid nitrogen flow system into and out of the chamber as well as a gas inlet valve to allow argon to be used as a shielding gas. Originally designed to accommodate vacuum conditions, the chamber suffered a degradation of the joint areas after several months of use. Therefore vacuum conditions were not simulated for this experiment. The chamber was, however, filled with argon gas to displace moisture and to help prevent condensation from freezing on the switch during testing.

4.4.1 Inside Chamber Test Configuration

Figure 4.6 shows the test configuration for the inside chamber testing.

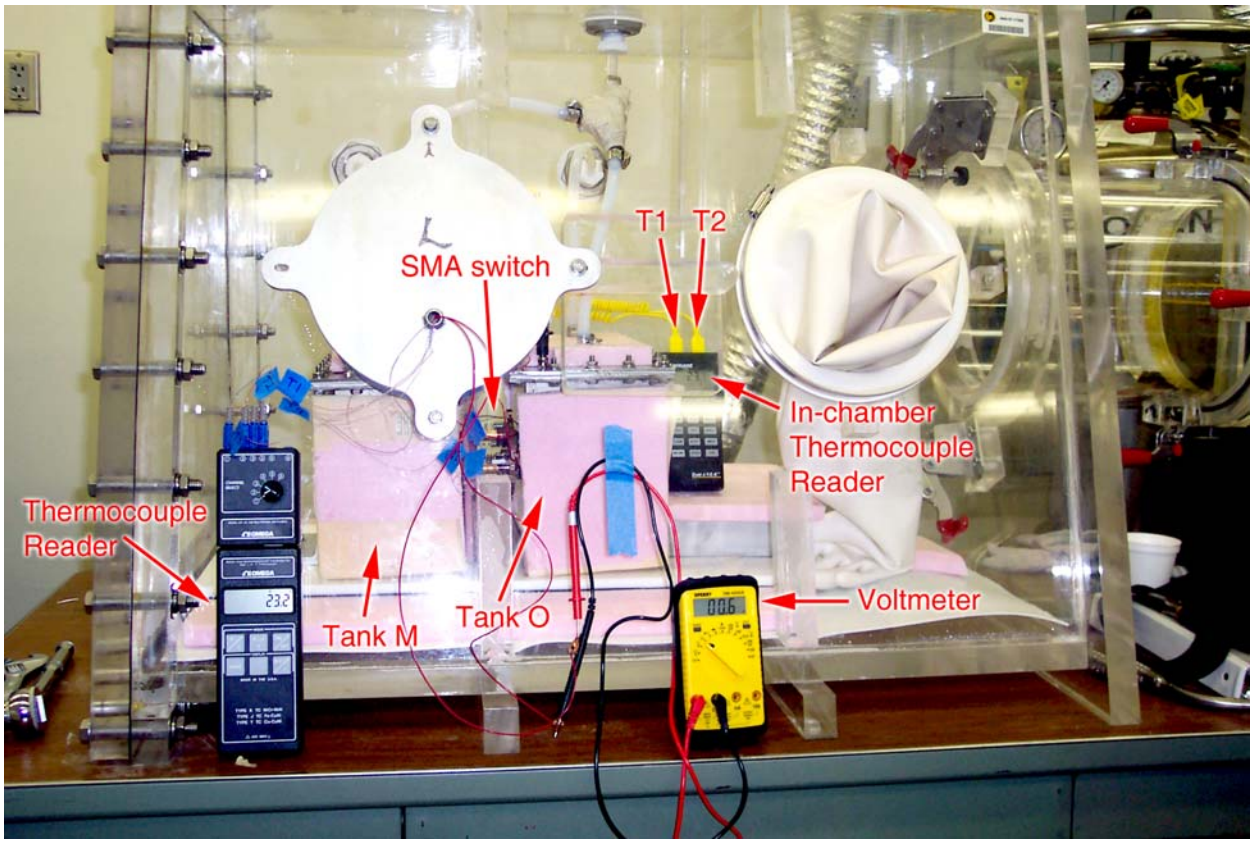

Figure 4.6: Inside chamber test configuration

Inside the chamber are two 8″ x 5″ x 7″ stainless steel tanks into which liquid nitrogen was allowed to flow through coils of copper tubing at different rates. As shown in Figure 4.7, the tanks have ports on their lids for a liquid nitrogen inlet and outlet, as well as a port to accommodate a thermocouple. They were filled with Syltherm XLT® cryogenic heat transfer fluid to help ensure efficient heat transfer between the liquid nitrogen coils and the sides of the tanks. The two tanks were maintained at two different temperatures to simulate the temperature difference between a liquid oxygen dewar and a liquid methane dewar. The switch was attached with three screws to the tank simulating the liquid methane dewar, and a layer of indium foil was placed between the switch and the side of the tank to help decrease the thermal contact resistance between the two surfaces. A copper disk covered with indium foil was attached to the mating

surface of the simulated oxygen dewar for the similar purpose of decreasing thermal contact resistance between the movable plate of the switch and the simulated oxygen dewar.

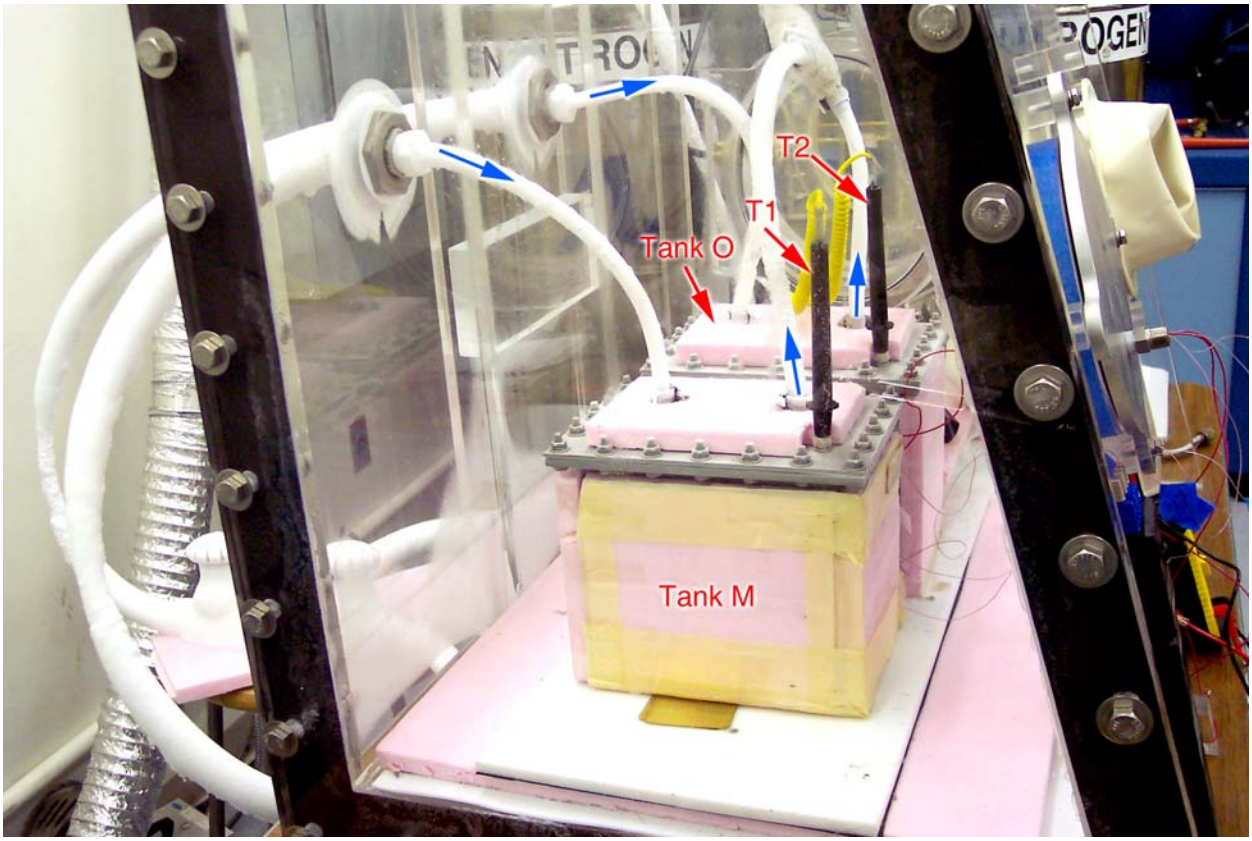

Figure 4.7: Side view of test chamber. Blue arrows indicate the flow of liquid nitrogen into Tank M and Tank O.

In addition to the thermocouples inserted into the two tanks, four more thermocouples were attached at various points across the switch. Since the displacement distance was expected to be small and therefore difficult to verify visually, voltmeter leads were attached to the simulated oxygen dewar and the movable plate on the switch. Resistance readings verified when contact was made between the two surfaces.

For in-chamber testing, three more bias springs were added to the configuration to help effect a greater displacement during actuation. The combined force of the additional springs was 11.39 N, in addition to the 20.73 N imparted by the central bias spring.

CHAPTER FIVE: RESULTS AND DISCUSSION

This chapter presents the results of the differential scanning calorimeter (DSC) experiments and the dilatometry data that were used to characterize the $Ni_{46.8}Ti_{50}Fe_{3.2}$ alloy. It also includes the experimental results of both the outside chamber and inside chamber testing of the thermal conduction switch.

5.1 Differential Scanning Calorimeter Testing

Four samples of $Ni_{46.8}Ti_{50}Fe_{3.2}$ with different heat treatments were tested using a Perkin-Elmer Diamond DSC. The samples were cut from strips of the alloy, which had been cut from the original billet of $Ni_{46.8}Ti_{50}Fe_{3.2}$ using electrical discharge machining (EDM). The samples were all tested in the DSC using the same temperature program: heat from –80 °C to 0 °C at 20 °C per minute, and cool from 0 °C to –80 °C at 20 °C per minute. The results are shown in Figure 5.1. The first sample, denoted by the black curve, received no heat treatment after being cut by EDM from the original billet. The second sample, denoted by the blue curve, received a solutionizing treatment of 850 °C for 30 minutes under vacuum and was subsequently furnace cooled. The third sample (orange line) was solutionized in the same manner as the second sample. Shape-setting was then attempted at 400 °C for 65 minutes, followed by water quenching. The final sample (green line) was solutionized using the same treatment as the second sample. It was then heat treated at 550 °C for 20 minutes, followed by water quenching in a second attempt at shape-setting. The shape-setting attempted to induce a pre-buckle in the cut strips.

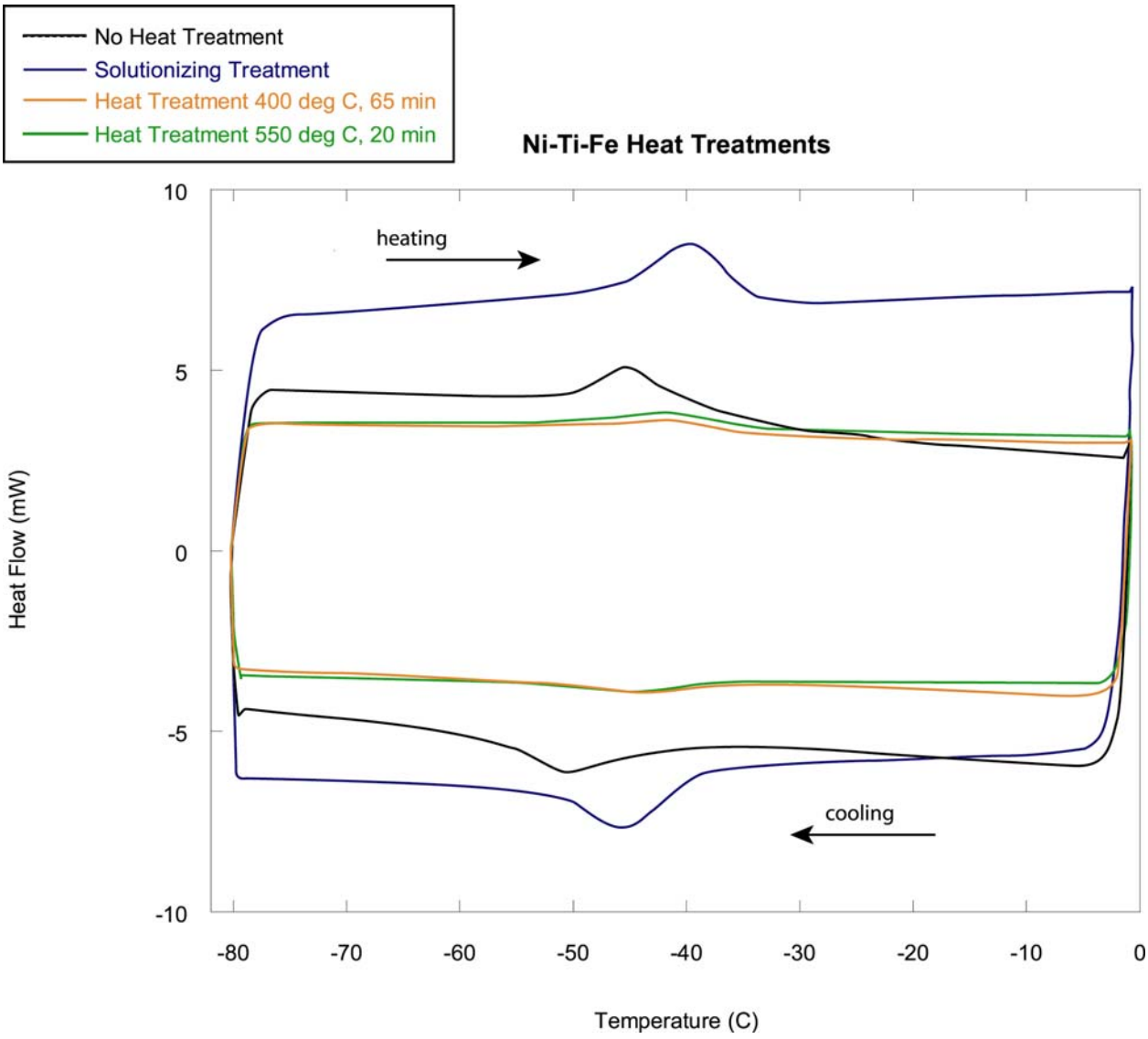

Figure 5.1: DSC curves for Ni-Ti-Fe heat treatments

The resulting data obtained from the DSC tests on the four samples is summarized in Table 5.1.

Table 5.1: DSC data for four Ni-Ti-Fe samples.

Heat Treatment	R-phase Transition Temperature (onset) (°C)	Austenitic Transition Temperature (onset) (°C)	Enthalpy of Transition (ΔH) (J/g)		Hysteresis (between peak temperatures) (°C)
			Cooling	Heating	
No heat treatment	-41.16	-51.05	-2.347	2.262	5.19
Solutionized at 850 °C / 30 min, vacuum cooled	-39.31	-45.72	-1.368	1.360	5.93
Solutionized, then 400 °C / 65 min, water quench	-37.90	-49.77	-1.003	1.089	3.54
Solutionized, then 550 °C / 20 min, water quench	-36.85	-49.74	-1.306	1.331	4.22

The hysteresis did not change significantly after the solutionizing treatment, and decreased only slightly after the subsequent heat treatments. Each subsequent heat treatment appeared to increase the onset temperature of the R-phase slightly while the austenitic onset temperature showed a significant increase only in the solutionized sample. The solutionizing treatment did result in a slightly sharper peak for the both the R-phase → austenite transition and the reverse transition. It also showed a decrease in the enthalpy for both transitions.

The heat treatments associated with both of the shape-setting attempts resulted in much broader peaks and less defined transition temperature regions. The strips that were heat treated at 400 °C for 65 minutes showed no evidence whatsoever that it had been "trained" into the pre-buckled shape that was intended in this attempt. The strips that underwent the 550 °C heat

treatment showed very minimal evidence of successful training into a pre-buckled shape. A possible explanation for the smaller peaks on the DSC curves is the disappearance of nickel-rich precipitates into the matrix of the material during the heat treatments. Since both of these samples were quenched after heat treatment, the precipitates were not permitted to grow. A disappearance of precipitates means fewer preferential nucleation sites from which the R-phase may grow. If further testing is able to confirm this trend, then successful shape-setting of Ni-Ti-Fe may require much higher temperatures, perhaps as high as the 850 °C solutionizing treatment.

5.2 Dilatometric Results

A sample of $Ni_{46.8}Ti_{50}Fe_{3.2}$ was cut from the original billet by EDM into a rectangular sample measuring 6 mm x 6 mm x 25 mm for testing in the liquid helium dilatometer. The sample was not solutionized or given any other heat treatment. The goal, as discussed in Chapter 3, was to look for a martensitic phase transformation in this alloy at temperatures down to –253 °C. The sample was cooled from room temperature down to –253 °C at approximately 3 °C/min, and subsequently heated back to room temperature at approximately 1.3 °C/min. The resulting temperature vs. sample length is shown in Figure 5.2. The difference in phase transformation onset temperatures in the heating and cooling curves suggests a thermal hysteresis of slightly less than 3 °C. This differs from the 5 °C hysteresis found in DSC testing for the un-heat-treated sample, but is within the margin of error for DSC temperature measurements. The 3 °C hysteresis indicated by the dilatometric results is more accurate, since it is indicative of the bulk response of the material. The DSC results, on the other hand, are susceptible in part to surface effects such as oxidation. The change in sample length during the phase transformation was

slightly more than 0.01mm. This change is lower than the expected 1% strain since the sample had not yet been shape-set, and the R-phase variants undergo self accommodation during cooling. The results confirm the presence and temperature range of the R-phase transformation, but no conclusive evidence of the presence of a martensitic transformation was discovered in this experiment.

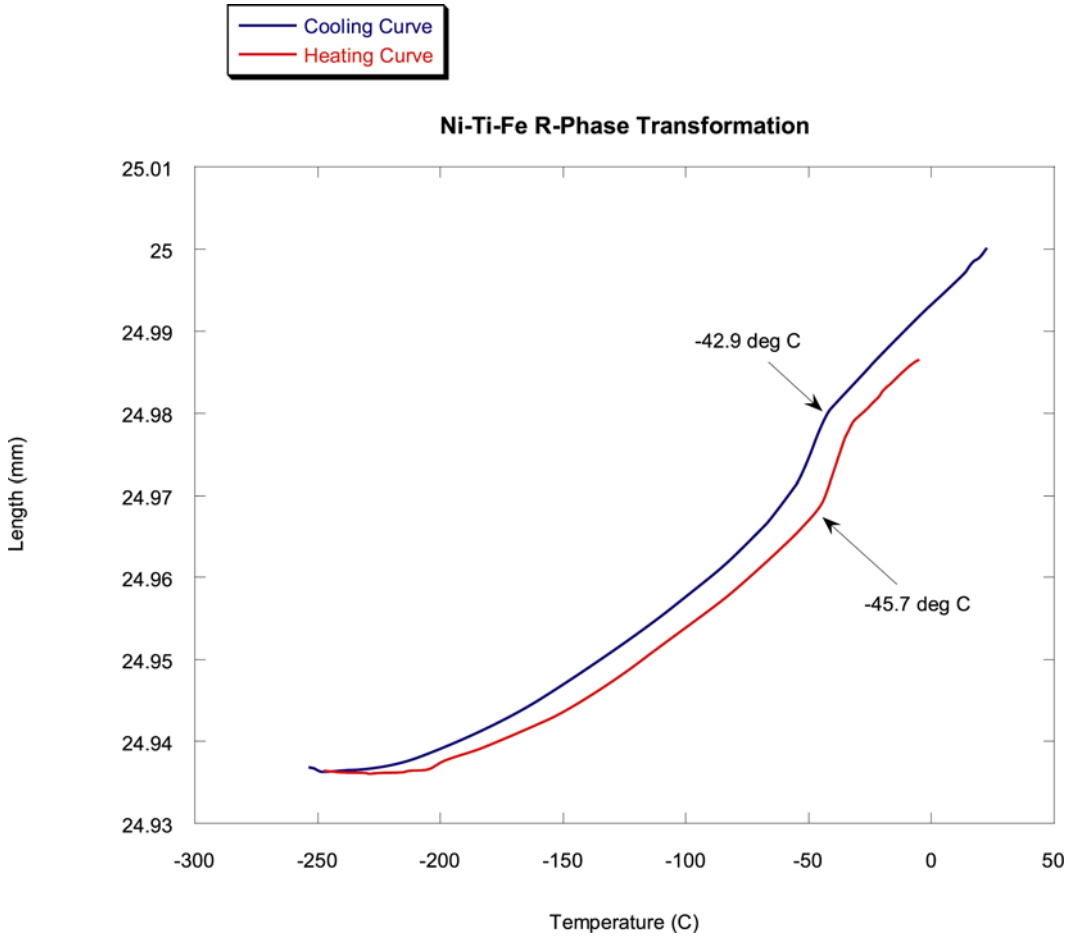

Figure 5.2: Temperature vs. length plot.

5.3 Outside Chamber Switch Actuation Results

The Ni-Ti-Fe thermal conduction switch was tested outside the chamber as described in Chapter 4. The strips installed in the switch were solutionized at 850 °C for 30 minutes and subsequently vacuum cooled, but were given no further heat treatments. Since separate shape-setting attempts were unsuccessful, the solutionizing treatment served as a shape-setting treatment and the strips were installed into the switch such that they had a slight pre-buckled shape at room temperature. This was accomplished by increasing the bias spring displacement, thereby increasing the force imparted to the strips, and by clamping the strips into the switch after cooling them in liquid nitrogen. The switch was slowly cooled to liquid nitrogen temperatures and allowed to warm back up to room temperature. Temperature vs. displacement data was recorded, and is shown in Figure 5.3.

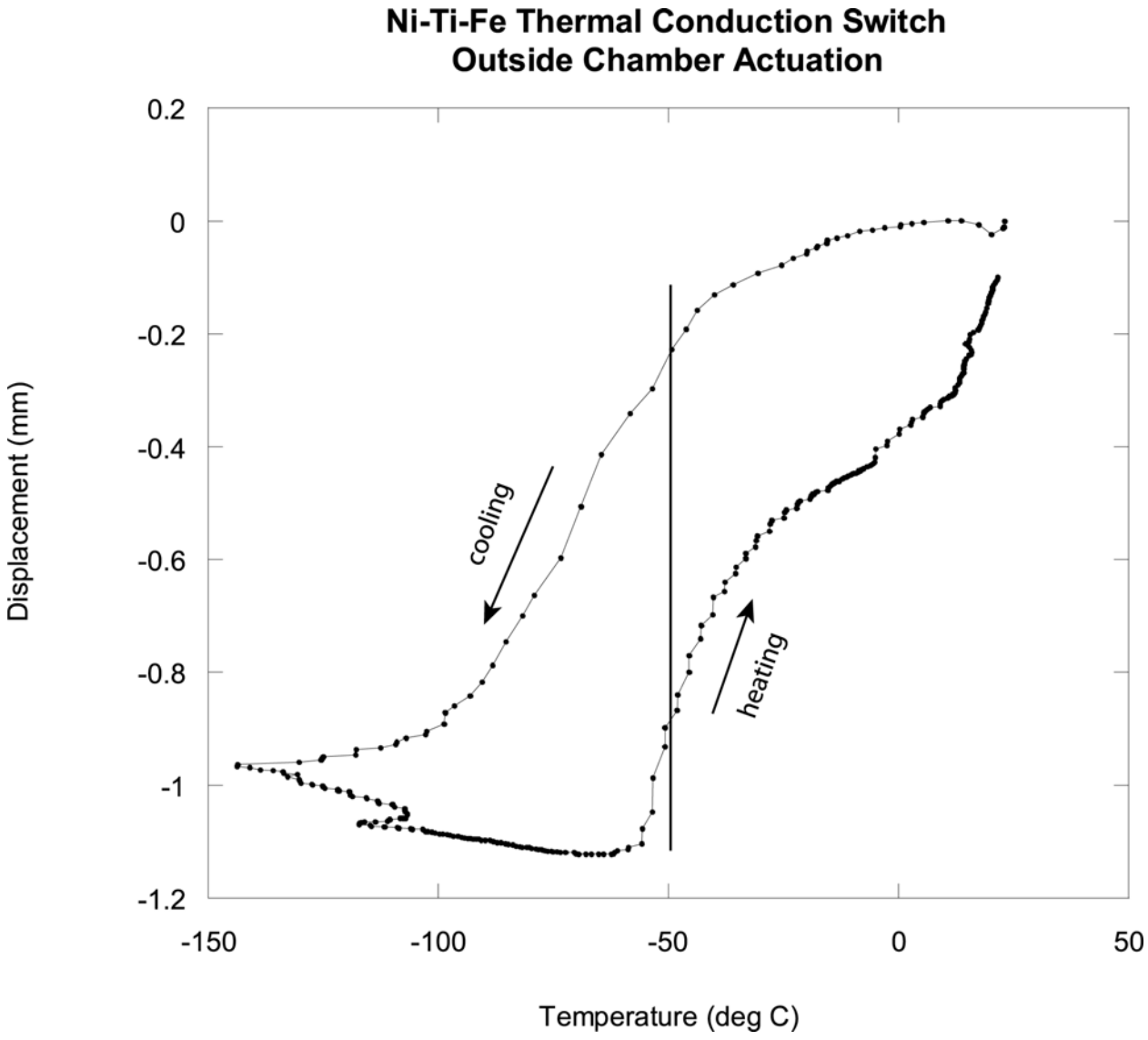

Figure 5.3: Outside chamber switch actuation: Temperature vs. Displacement.

Accurate measurements of transformation temperature onset were difficult due to the large thermal gradient across the entire length of the strips. While the upper portion of the switch and the strips heated above the R-phase transformation temperature relatively quickly, the lower portion of the strips remained below the transformation temperature. In terms of characterization of the Ni-Ti-Fe strips, the DSC and dilatometer data are more accurate means of determining

transformation temperatures. However, the plot in Figure 5.3 gives a good overall idea of the switch performance during thermal cycling.

5.3.1 Testing Issues

Several issues were encountered during the course of the outside chamber experiments which affected both accurate data acquisition and switch performance. These issues were identified and remedied, and are discussed in this section.

5.3.1.1 Thermocouple Placement

The thermocouple was attached to one of the Ni-Ti-Fe strips to directly measure the temperature of the alloy during the cycle. Placement of the thermocouple proved to be somewhat problematic, since a very large temperature gradient was induced along the length of the strip. Several trials were conducted during which the placement of the thermocouple was varied. If it was placed too close to the top of the switch, which warmed up much more quickly than the bottom of the strip, the temperature vs. displacement data was shifted to make it appear as though the phase transformation was happening at a much higher temperature. If the thermocouple was attached too close to the bottom of the switch, then it was in direct contact with the liquid nitrogen, which caused the temperature reading to reach its minimum (the temperature of liquid nitrogen) before the switch had finished actuating. This had the effect of making it appear falsely that the majority of the displacement was occurring at the minimum temperature. When the thermocouple was located approximately 1/3 of the length of the strip from the bottom plate, the resulting data showed a nearly constant slope in the temperature vs.

displacement plot. This occurred because the bottom 1/3 of the strip was still becoming too cold too quickly, and warming up too slowly to be accurately associated with the overall switch displacement. Successful results were obtained when the thermocouple was attached just below the halfway point on the Ni-Ti-Fe strip.

5.3.1.2 Lubricants

The relatively close tolerance between the support rods and the bearings in the top plate of the switch required use of a lubricant to help prevent the switch from binding during actuation. Initially, Syltherm XLT® (Cryogenic Heat Transfer Fluid) was used as a lubricant between the support rods and bearings. Several experimental runs using the Syltherm resulted in total deflections of 0.1 – 0.3 mm, which was determined to be within the range of observable thermal contraction of the copper at liquid nitrogen temperatures. Investigation revealed that Syltherm XLT® freezes at –111 °C, which is well above liquid nitrogen temperature.

A second lubricant, Apezion N grease, was then tested. Commercial specs of this product indicated it was effective at temperatures well below that of liquid nitrogen. When the next group of experiments revealed similarly small total deflections, the lubrication itself was tested in liquid nitrogen. When exposed to this temperature, the Apezion N grease became brittle and hard, which indicated that it was also inhibiting the switch actuation.

Finally, a chemically pure PTFE aerosol (Teflon®) was applied to the moving parts. This lubricant allowed uninhibited movement of the switch, and proved to produce the most successful test results.

5.3.1.3 Configurational Stability

The switch, which was designed to accommodate up to six SMA strips, was originally tested with only two Ni-Ti-Fe strips located on opposite sides. The removal of the third strip was done in order to maximize the deflection of the switch while still maintaining configurational symmetry. While this configuration did, in fact, result in greater overall deflections, the top plate of the switch had a tendency to wobble back and forth in the direction parallel to the strip width. This instability occasionally resulted in binding of the switch during actuation, so a third strip was added to the configuration. This resulted in approximately a 30% reduction in overall switch displacement, but the displacement results were more consistent with this configuration.

5.4 Inside Chamber Switch Actuation Results

The Ni-Ti-Fe switch was tested inside the testing chamber as described in Chapter 4. Temperature data points were taken at 15-minute intervals for the tank simulating the liquid methane, “Tank M”, the tank simulating the liquid oxygen, “Tank O”, and for each of four thermocouples installed at points across the switch. Thermocouples T1 and T4 were installed on the fixed and movable copper base plates of the switch, respectively. Thermocouples T2 and T3 were attached to two central points on the SMA strip, distanced approximately 2 cm apart. The resulting data is shown in Figure 5.4.

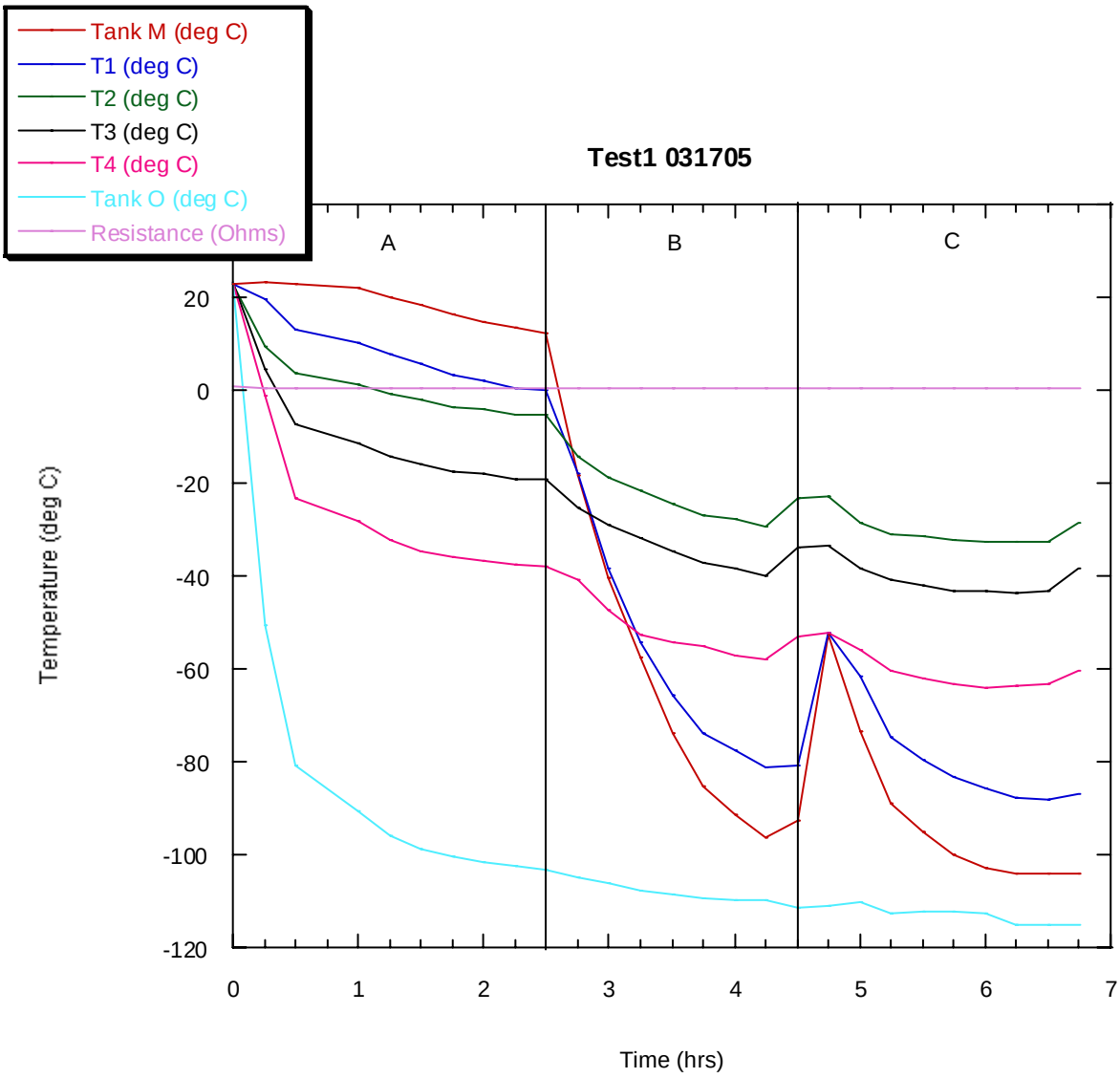

Figure 5.4: Inside chamber test results

For the first test run, liquid nitrogen was allowed to flow into Tank O, while the valve for Tank M was kept closed. For 2.5 hours (section "A" in Figure 5.4), Tank M was cooled only by means of conduction through the switch, which was in thermal contact with both tanks (closed position). With this data, the heat flow rate through the switch was calculated. The specific heat

of the Syltherm XLT® heat transfer fluid is 1339 J/kg-K, and the mass of this fluid in Tank M was found to be 3.343 kg. This allows the heat flow rate across the switch to be calculated for section "A" according to equation 10:

$$Q = \frac{m \cdot c_p \cdot \Delta T}{\Delta t} \tag{10}$$

where m is the mass of the fluid in Tank M, c_p is the specific heat of the Syltherm, ΔT is the temperature change of the fluid in Tank M, and Δt is the length of time over which ΔT is measured. The average value for ΔT of Tank M in section "A" was –1.375 °C. With an average Δt of 900 seconds, this gives an average heat flow rate of 6.8 W.

The average temperature difference between Tank M and Tank O during the time period in section "A" was –109.86 °C. Since the requirements dictate a 28 K difference in temperature between Tank M and Tank O, and this temperature difference was much higher during this portion of the test, the heat transfer rate was extrapolated for a 28 K temperature difference and found to be 1.7 W (average). This is below the 8 W requirement, and may be due in part to any or all of the following: 1) Low contact force between the switch and Tank O. Since the expected actuation distance is small with this particular switch configuration, any additional contact force which buckles the strips beyond their expected actuation distance will prevent effective movement of the switch; 2) Application of PTFE aerosol (Teflon®) to the switch support rods. While this worked effectively as a lubricant, Teflon® also acts as an insulator, which may have reduced the effective heat transfer across the switch components; and 3) Convection inside the chamber. While precautions were taken to ensure appropriate test conditions, the effects of convective heat transfer at cryogenic temperatures are much more pronounced.

During section “B” in Figure 5.4, the valve for Tank M was opened, and liquid nitrogen was allowed to cool the tank directly in order to expedite the switch actuation process. At the transition point between section “B” and section “C”, the first tank of liquid nitrogen was emptied and the system was connected to a second tank. During the few minutes required for the transfer, the entire system began to heat up, as shown by the peaks in section “C”.

5.4.1 Thermal Gradients

During the first test, a large temperature gradient was noted across the length of the SMA strips. Temperature gradients invariably develop along the conduction path, which cause partial phase transformation across some areas of the SMA strips. This can prove somewhat problematic when the temperature gradient is large, since the complete phase transformation will occur over a much larger period of time. Figure 5.5 shows the temperature gradient vs. time across the length of the SMA strips during three separate tests.

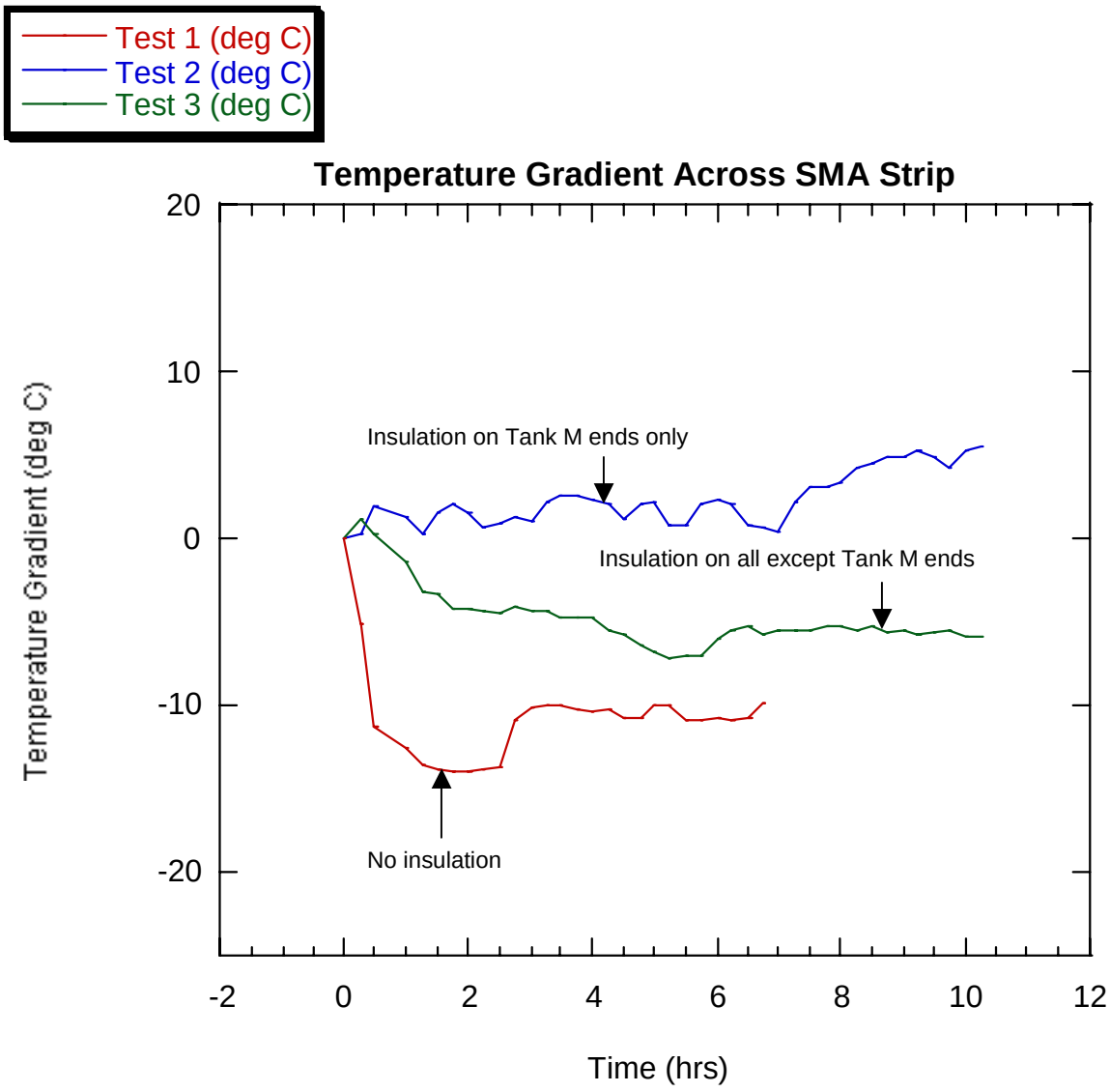

Figure 5.5: Thermal gradient across the SMA strip.

Figure 5.5 helps to illustrate the effectiveness of insulation placement on the SMA strips as a means of reducing the thermal gradient. During Test 1, no insulation was placed on the SMA strips. For Test 2, the ends of the strips closest to Tank M were insulated with Teflon® tape. The strips in Test 3 were completely coated with a single layer of Teflon® tape except the ends

closest to Tank M. The ends closest to Tank O had a thicker layer of the tape applied to them. Figure 5.5 shows the smallest thermal gradient magnitude associated with Test 2. However, since the temperature difference between Tank M and Tank O during the tests also factors into the magnitude of the thermal gradient across the switch, this must also be considered. The relevant temperature data from the three tests are presented in Table 5.2.

Table 5.2: Thermal gradient data for inside chamber tests.

Test	**ΔT across SMA Strip |T3 – T2| (average) (°C)**	**ΔT |Tank O – Tank M| (average) (°C)**	**Thermal Gradient Index |(T3-T2)/(Tank O-Tank M)|**
Test 1	10.57	34.41	0.31
Test 2	2.58	18.47	0.14
Test 3	4.76	7.82	0.61

When the overall temperature difference between the two tanks is considered, the lowest thermal gradient index resulted from the insulation configuration in Test 2. The gradient indexes from Tests 1 and 3 may seem at first to be contradictory. However, during Test 1 there was a greater contact force between the switch and Tank O than during Test 3. The larger contact force allows the temperature difference between the two tanks to have a greater influence on the strip thermal gradient. During Test 3, the less extreme temperature difference between Tank M and Tank O should have caused a smaller thermal gradient across the strip. However, the insulation on the strips at the Tank O end actually *caused* a greater thermal gradient across the strip. If the

insulation had not been present in this case, Tank O would have further cooled the ends of the strips closest to it, and therefore reduced the gradient.

CHAPTER SIX: CONCLUSIONS AND RECOMMENDATIONS

6.1 Conclusions

The characterization and testing of a $Ni_{46.8}Ti_{50}Fe_{3.2}$ shape memory alloy has been presented as part of the ongoing efforts to develop and improve upon the design of a shape memory alloy thermal conduction switch to fulfill a NASA-KSC requirement for passive thermal control at cryogenic temperatures. A new switch configuration was tested which used low hysteresis SMA strips as the actuation elements. The feasibility of utilizing a Ni-Ti-Fe alloy as an actuation element in a cryogenic thermal conduction switch configuration has been demonstrated. A liquid helium dilatometer was commissioned for future use in low-temperature materials characterization, and recommendations were made for improvements to the system and for running the system with liquid nitrogen as an alternate cryogen. The $Ni_{46.8}Ti_{50}Fe_{3.2}$ alloy was characterized by DSC measurements and liquid helium dilatometry, and verified to have a low hysteresis. A finite element analysis was conducted on a single strip of the alloy with the applied force imparted by the switch's bias spring in order to produce a stress profile which helped to clarify the influence of the stress gradient on the phase transformation. Strips of the Ni-Ti-Fe alloy were fabricated and installed into the thermal conduction switch, and the overall performance of the switch in terms of deflection, hysteresis, and heat flow rate was evaluated. Low hysteresis actuation was confirmed, and a small deflection associated with the R-phase change was noted. Recommendations have been made for improvement upon thermal conduction switch testing conditions and switch design configuration, and are discussed in section 6.2.

6.2 Recommendations

1) The current switch configuration utilizes SMA actuating elements in the shape of pre-buckled strips. While this has the advantage of ease of fabrication, it is limiting in terms of actuator design options. The ability to successfully shape-set $Ni_{46.8}Ti_{50}Fe_{3.2}$ would be extremely advantageous in this regard. Since both attempts at separate shape-setting heat treatments described in Chapter 5 were not successful, it is recommended to attempt a combined solutionizing and shape-setting treatment of those strips. If such heat treatments result in a DSC peak similar to the solutionized sample in Figure 5.1, it will be clear that higher temperatures should be pursued for successful shape-setting of $Ni_{46.8}Ti_{50}Fe_{3.2.}$
2) Another limitation to the current switch design is the 1% strain limitation of shape memory alloys undergoing the austenite → R-phase and the reverse transitions. The buckled strip configuration produces a very small deflection. In order to compensate for this, an alternate shape memory element configuration, perhaps along the lines of a helical spring, should be used to help increase mechanical advantage. The ability to successfully shape-set the $Ni_{46.8}Ti_{50}Fe_{3.2}$ alloy would increase the possibilities for additional design configurations.
3) The thermal gradient that develops across the conduction path of the switch during operation has proven problematic. It causes non-uniform phase changes across the length of the actuation element, which can therefore inhibit full deflection of the switch. Design of a switch that minimizes the thermal gradient is being pursued.
4) A new testing chamber which can sustain vacuum conditions is required for more accurate simulation of switch operation conditions. This will eliminate convective heat transfer

during the testing, and will prevent all frost from forming inside the chamber on the switch and tank surfaces.

REFERENCES

Canales A., Morales F., Escudero R. and Rios-Jara D., "Electric Transport Properties of the B2 to R Phase Transition in TiNiFe Alloy", Journal de Physique III, Volume 5, (1995), pp. C2-99 – C2-103.

Droney, M., Kaiboussi, N., Lemanski, J., Rodriguez, C. and Woodruff, T., Senior Design Project Report, "Shape Memory Alloy Thermal Switch", University of Central Florida, 2003.

Goo E., Duerig T., Melton K., and Sinclair R., "Mechanical Twinning in $Ti_{50}Ni_{47}Fe_3$ and $Ti_{49}Ni_{51}$ Alloys", *Acta Metall*. Vol. 33, No. 9, (1985), pp. 1725-1733.

Honma T., "2.1: TiNi-Based Shape Memory Alloys", in *Shape Memory Alloys*, edited by H. Funakubo, Gordon and Breach Science Publishers, New York, 1984, pp. 61-115.

Humbeeck J. V., "Shape Memory Alloys: A Material and a Technology", Advanced Engineering Materials, Vol. 3, No. 11, (2001), pp. 837-850.

Hwang C. M. and Wayman C. M., "Compositional Dependence of Transformation Temperatures in Ternary TiNiAl and TiNiFe Alloys", *Scripta Metallurgica*, Vol. 17, (1983), pp. 381-384.

Hwang C. M., Meichle M., Salamon M. B., and Wayman C. M., "Transformation Behaviour of a $Ti_{50}Ni_{47}Fe_3$ Alloy: I. Premartensitic Phenomena and the Incommensurate Phase", *Philosophical Magazine A*, Vol. 47, (1983), pp. 9-29.

Hwang C. M., Meichle M., Salamon M. B., and Wayman C. M., "Transformation Behaviour of a $Ti_{50}Ni_{47}Fe_3$ Alloy: II. Subsequent Premartensitic Behaviour and the Commensurate Phase", *Philosophical Magazine A*, Vol. 47, (1983), pp. 31-62.

Hwang C. M., Salamon M. B., and Wayman C. M., "Transformation Behaviour of a $Ti_{50}Ni_{47}Fe_3$ Alloy: III. Martensitic Transformation", *Philosophical Magazine A*, Vol. 47, (1983), pp. 177-193.

Hwang C. M., Meichle M., Salamon M. B., and Wayman, C. M., "Phase Changes in a $Ti_{50}Ni_{47}Fe_3$ Alloy", *Res Mechanica* 10 (1984) pp. 1-23.

Jiang C. and Xu H., "Effect of Pre-Deformation on Hysteresis in TiNiFe Shape Memory Alloys", Proceedings of the International Symposium on Shape Memory Materials, Kanazawa, Japan, May (1999), pp. 111-114.

Jiang C. and Xu H., "Effect of Pre-Deformation on the Transformation Temperatures of TiNi Shape-Memory Alloys", Materials Science Forum, Vols. 394-395, (2002), pp. 269-272.

Jiménez M., Aburto S., Gómez R., Marquina V., Marquina M. L., and Ríos-Jara D., "Premartensitic Phase Transformation in a TiNiFe Shape Memory Alloy Studied by Mössbauer Spectroscopy", *Hyperfine Interactions*, Vol. 66, (1991), pp. 345-350.

Jinfang G., Yuying C., Ming A., Long S., and Guansen Y., "The Influence of Thermomechanical Treatment on R-phase Transition and Shape Memory Effect", Materials Research Society Symposium Proceedings, Vol. 246, (1992), pp. 1-10.

Krishnan V. B., Thesis, "Design, Fabrication and Testing of a Shape Memory Alloy Based Cryogenic Thermal Conduction Switch", University of Central Florida, 2003.

Krishnan V. B., Singh J. D., Woodruff T. R., Notardonato W. U. and Vaidyanathan R., "A Shape Memory Alloy Based Cryogenic Thermal Conduction Switch", *Advances in Cryogenic Engineering - Transactions of the International Cryogenic Materials Conference - ICMC*, Vol.50, American Institute of Physics (2004), pp. 26-33.

McMordie R. and Panetti A., "11.5 Thermal" in Chapter 11 of Space Mission Analysis and Design, Third Edition, edited by Wertz J. and Larson W., Microcosm Press and Kluwer Academic Publishers, 1999, pp. 428-458.

Miyazaki S., and Otsuka K., "Deformation and Transition Behavior Associated with the R-phase in Ti-Ni Alloys", Metallurgical Transactions A, Vol. 17A, (1986), pp. 53-63.

Moberly W. J., Proft J. L., Duerig T. W., and Sinclair R., "Deformation, Twinning and Thermo-Mechanical Strengthening of $Ti_{50}Ni_{47}Fe_3$", *Acta Metall Mater*, Vol. 38, No. 12, (1990), pp. 2601-2612.

Ohkata I. and Suzuki Y., "Chapter 11: The Design of Shape Memory Alloy Actuators and their Applications" in *Shape Memory Materials*, edited by Otsuka K. and Wayman C. M., Cambridge University Press, 1998, pp. 240-266.

Otsuka K. and Ren X., "Factors Affecting the M_s Temperature and its Control in Shape-Memory Alloys", *Materials Science Forum*, Vol. 394-395, (2002), pp. 177-184.

Otsuka K. and Wayman M., "Chapter 2: Mechanism of Shape Memory Effect and Superelasticity" in *Shape Memory Materials*, edited by Otsuka K. and Wayman C. M., Cambridge University Press, 1998, pp. 27-48.

Oxford Instruments, OptistatCF Operator's Handbook, England, 2003.

Perkins J. and Hodgson D., "The Two-Way Shape Memory Effect", in *Engineering Aspects of Shape-Memory Alloys*, edited by Duerig, T. W., Melton, K. N., Stöckel, D. and Wayman, C. M., Butterworth-Heinemann, London, 1990, pp. 195-206.

Ren X., Miura N., Zhang J., Otsuka K., Tanaka K., Koiwa M., Suzuki T., Chumlyakov Yu.I., and Asai M., "A Comparative Study of Elastic Constants of Ti-Ni-based Alloys Prior to Martensitic Transformation", *Materials Science and Engineering* Vol. A312, (2001), pp. 196-206.

Saburi T., "Chapter 3: Ti-Ni Shape Memory Alloys" in *Shape Memory Materials*, edited by K. Otsuka and C.M. Wayman, Cambridge University Press, 1998, pp. 49-96.

Schetky, L. M., "Shape Memory Alloy Applications in Space Systems", in *Engineering Aspects of Shape-Memory Alloys*, edited by Duerig, T. W., Melton, K. N., Stöckel, D. and Wayman, C. M., Butterworth-Heinemann, London, 1990, pp. 170-178.

Shmalo, S., "Neutron Diffraction Investigation of Deformation in Ni-Ti-Fe", University of Central Florida, (work in progress).

Tautzenberger, P., "Thermal Actuators: A Comparison of Shape Memory Alloys with Thermostatic Bimetals and Wax Actuators", in *Engineering Aspects of Shape-Memory Alloys*, edited by Duerig, T. W., Melton, K. N., Stöckel, D. and Wayman, C. M., Butterworth-Heinemann, London, 1990, pp. 207-218.

Theta Industries, Inc., Operation Manual for Project #P511, 2003.

TiNi Aerospace, Inc., San Leandro, CA, http://www.tiniaerospace.com/about.html.

Tobushi H., Yamada S., Hachisuka T., Ikai A., and Tanaka K., "Thermomechanical Properties due to Martensitic and R-phase Transformations of TiNi Shape Memory Alloy Subjected to Cyclic Loadings", *Smart Mater. Struct.* **5,** 1996, pp. 788-795.

Uchil, J., "Shape Memory Alloys – Characterization Techniques", Pramana Journal of Physics, Vol. 58, Nos 5 & 6, 2002, pp. 1131-1139.

Voggenreiter H., Schuster A., Mertmann M., Reindl M., Roth M., and Vorbrugg H., "Shape Memory Based Release Mechanism for Satellite Devices", Proceedings of the 33rd Aerospace Mechanisms Symposium, Pasadena CA, 1999, pp. 169-174.

Wayman C. M. and Duerig T. W., "An Introduction to Martensite and Shape Memory", in *Engineering Aspects of Shape-Memory Alloys*, edited by Duerig, T. W., Melton, K. N., Stöckel, D. and Wayman, C. M., Butterworth- Heinemann, London, 1990, pp. 3-20.

Xu H., Jiang C., Gong S., and Feng G., "Martensitic Transformation of the $Ti_{50}Ni_{48}Fe_2$ Alloy Deformed at Different Temperatures", *Materials Science and Engineering* A281, 2000, pp. 234-238.